

Zero-Prandtl-number convection with slow rotationPriyanka Maity¹ and Krishna Kumar^{1, a)}*Department of Physics, Indian Institute of Technology, Kharagpur-721 302,
India*

(Dated: 25 May 2022)

We present the results of our investigations of the primary instability and the flow patterns near onset in zero-Prandtl-number Rayleigh-Bénard convection with uniform rotation about a vertical axis. The investigations are carried out using direct numerical simulations of the hydrodynamic equations with stress-free horizontal boundaries in rectangular boxes of size $(2\pi/k_x) \times (2\pi/k_y) \times 1$ for different values of the ratio $\eta = k_x/k_y$. The primary instability is found to depend on η and Ta . Wavy rolls are observed at the primary instability for smaller values of η ($1/\sqrt{3} \leq \eta \leq 2$ except at $\eta = 1$) and for smaller values of Ta . We observed Küppers-Lortz (KL) type patterns at the primary instability for $\eta = 1/\sqrt{3}$ and $Ta \geq 40$. The fluid patterns are found to exhibit the phenomenon of bursting, as observed in experiments [Bajaj et al. Phys. Rev. E **65**, 056309 (2002)]. Periodic wavy rolls are observed at onset for smaller values of Ta , while KL-type patterns are observed for $Ta \geq 100$ for $\eta = \sqrt{3}$. In case of $\eta = 2$, wavy rolls are observed for smaller values of Ta and KL-type patterns are observed for $25 \leq Ta \leq 575$. Quasi-periodically varying patterns are observed in the oscillatory regime ($Ta > 575$). The behavior is quite different at $\eta = 1$. A time dependent competition between two sets of mutually perpendicular rolls is observed at onset for all values of Ta in this case. Fluid patterns are found to burst periodically as well as chaotically in time. It involved a homoclinic bifurcation. We have also made a couple of low-dimensional models to investigate bifurcations for $\eta = 1$, which is used to investigate the sequence of bifurcations.

Keywords: Rotating zero-Prandtl-number convection, pattern-forming instability, self-tuned waves, homoclinic bifurcation

^{a)}Electronic mail: kumar@phy.iitkgp.ernet.in

I. INTRODUCTION

Thermal convection in low-Prandtl-number ($Pr \ll 1$) fluids¹⁻¹⁵ is widely investigated due to its relevance in the study of convective zones in stars and the Sun ($Pr \sim 10^{-8}$), Earth's molten core⁴ ($Pr \sim 10^{-1}$), liquid metals⁵ ($Pr \sim 10^{-3} - 10^{-2}$), and pattern-forming instabilities⁶⁻¹⁵. Rayleigh-Bénard convection¹⁶, which consists of a thin horizontal fluid layer uniformly heated from below and uniformly cooled from above, is a simplified version to study the complexities of thermal convection. The convection in a Boussinesq fluid is governed by two nonlinearities: the self-interaction of the velocity field $(\mathbf{v} \cdot \nabla)\mathbf{v}$ and the advection of temperature by the velocity field $(\mathbf{v} \cdot \nabla)\theta$. Proctor² suggested two different flow regimes for the convection near the instability onset in low-Prandtl-number fluids: the inertial and the viscous regimes. If $(\mathbf{v} \cdot \nabla)\mathbf{v}$ is nonzero but compensated by the pressure gradient, the flow dynamics is described by the nonlinear term $(\mathbf{v} \cdot \nabla)\theta$. The convective heat flux $(Nu - 1)$ across the fluid layer could be large and independent of Pr . The corresponding convection is said to be in the inertial regime. If the convective heat flux is small and $Nu - 1 \sim Pr^2$, the corresponding convection is said to be in the viscous regime. Chiffaudel, Fauve & Perrin⁵ established the existence of these two flow regimes experimentally. The asymptotic form of the Boussinesq equations for Rayleigh-Bénard convection in the zero-Prandtl-number ($Pr \rightarrow 0$) limit was proposed by Spiegel¹⁷ to simplify the study of convective turbulence in an astrophysical context. The nonlinear term $(\mathbf{v} \cdot \nabla)\theta$ is neglected in this limit, and the thermal convection is described by the term $(\mathbf{v} \cdot \nabla)\mathbf{v}$. This limit is therefore the viscous regime of convection. The only nonlinearity $(\mathbf{v} \cdot \nabla)\mathbf{v}$ is unable to saturate two-dimensional (2D) rolls, as the 2D growing rolls become the exact nonlinear solution with *stress-free* horizontal boundaries. This makes the $Pr \rightarrow 0$ limit with stress-free boundary conditions a singular limit. Thual¹² showed the saturation of thermal convection in direct numerical simulations (DNS) of three-dimensional (3D) flows in this limit with stress-free boundaries. A simple model for a possible saturation mechanism of the instability was suggested by Kumar, Fauve & Thual¹⁸, which also showed the possibility of critical bursting¹⁹ at the primary instability. Recent studies¹³ show several interesting instabilities including a homoclinic bifurcation close to the primary instability. The strong similarity of convective flows^{14,15} for very small values of Pr with those of Spiegel's equations^{12,13} confirm the existence of a smooth $Pr \rightarrow 0$ limit.

Rotation about a vertical axis^{16,20-32} introduces the centrifugal force and the Coriolis

force. Both the forces act along the horizontal plane. The centrifugal force^{31,33} introduces large scale circulation into the flow and modifies the temperature profile of the basic state. The Froude number Fr , which is the ratio of the centrifugal force and the buoyancy force, becomes an important parameter for the fluid flow. Lopez and Marques³¹ investigated the effects of centrifugal force on fluid flow in detail. The Coriolis force linearly couples the vertical velocity and the vertical vorticity. This delays the onset of Rayleigh-Bénard convection¹⁶, affects the heat flux^{23,24,34-40} across the fluid layer, and breaks the mirror-symmetry of the convective flow even at small rotation rates. The Coriolis force also affects the turbulent spectra⁴¹. Chandrasekhar¹⁶ analyzed the linear problem considering only the Coriolis force and showed that the infinitesimal convection always appeared as stationary convection, if $Pr > 0.677$. He predicted oscillatory convection at onset if $Pr < 0.677$ and if Ta is greater than a critical value $Ta_o(Pr)$. Küppers & Lortz (KL)^{21,22} investigated the nonlinear convection and showed that the flow was always unsteady at onset if Ta is greater than a threshold $Ta_{KL}(Pr) < Ta_o(Pr)$. A set of rolls is then replaced by a new set of rolls of the same wavelength but oriented approximately at an angle of 60° with the old set^{42,43} at the onset. Recent studies on pattern-forming instabilities^{26,30,31,44-47} showed interesting patterns. Square patterns^{30,44,47} were also observed in presence of rotation. Bajaj et al.⁴⁵ observed bursts of finite-amplitude rolls which appeared and then disappeared at almost regular intervals. Clever & Busse²⁶ also observed bursting of the convective heat flux in simulations of oscillatory convection with no-slip boundary conditions, while Dawes²⁸ found bursting in a model of convection near a bicritical point with stress-free boundary conditions. Not much is known, however, about the phenomenon of bursting of patterns in the regime of stationary convection in a rotating Rayleigh-Bénard system.

We present in this article the results of a detailed investigation of the fluid patterns near the primary instability in a Rayleigh-Bénard system rotating uniformly but slowly about a vertical axis in the $Pr \rightarrow 0$ limit. This work is motivated by our curiosity concerning the effect of Coriolis force on the pattern dynamics close to the onset of Rayleigh-Bénard convection in very low-Prandtl-number fluids. The purposes of this paper are twofold. The first is to investigate Küppers-Lortz (KL) instability in very low-Prandtl-number fluids. The second purpose is to explore the effects of the Coriolis force on the phenomenon of critical bursting, which is observed in low-Prandtl-number fluids. We carried out direct numerical simulations (DNS) of the hydrodynamical system with *stress-free* boundary conditions in a

three-dimensional simulation box of size $2\pi/k_x \times 2\pi/k_y \times 1$ for a wide range of Taylor numbers Ta . The ratio $\eta = k_x/k_y$ was varied in a range $1/\sqrt{3} \leq \eta \leq 10$. The convection is found to be always three-dimensional and time dependent at the primary instability. Irregular bursts of waves were excited along the roll axis in larger boxes, whenever the amplitude of rolls exceeded a critical value for $\eta > 2$. This led to the possibility of chaotic bursting of oblique rolls for $\eta > 2$. For $\eta = 2$, we observed wavy rolls for $Ta \leq 10$ and chaotic oblique rolls for $Ta > 10$ near the instability onset. We observed an interesting competition between two sets of mutually perpendicular rolls in a square simulation box ($\eta = 1$), which shows irregular and regular bursting of fluid patterns. A sequence of inverse homoclinic gluing, inverse Hopf and inverse pitchfork bifurcations was also observed in a small square box, when the Rayleigh number Ra was raised in small steps for a fixed value of Ta . Fluid patterns showed periodic as well as chaotic bursting. Küppers and Lortz (KL) patterns²¹ are observed at the onset for certain range of Ta , which depend on the ratio η . For $\eta \geq 4$, the convection is found to be chaotic at the onset even for smaller values of Ta . A set of wavy rolls is replaced irregularly in time by a new set of oblique wavy rolls of different wavelength at onset. We have also constructed a couple of low-dimensional models for $\eta = 1$, which captures qualitatively the flow patterns observed in DNS for smaller values of Ta and the reduced Rayleigh number r .

II. HYDRODYNAMIC PROBLEM

We consider a thin horizontal layer of Boussinesq fluid of thickness d , kinematic viscosity ν , thermal expansion coefficient α , thermal diffusivity κ , rotating uniformly with angular velocity Ω about a vertical axis. The fluid layer is heated uniformly from below and cooled uniformly from top to maintain an adverse temperature gradient β across the fluid layer. The Froude number $Fr = \Omega^2 L/g$ is always less than 2.2×10^{-3} for the rotation rates considered here ($Ta \leq 700$). The effects of centrifugal force are therefore ignored here. We have called the rotation rates slow, as we have considered the simulations for smaller values of Ta such that the effects of the centrifugal force may be ignored. It is then possible to have stationary conduction as a basic state in the rotating frame of reference. The convective flow, in the Boussinesq approximation, is then governed by the following set of dimensionless equations:

$$\partial_t \mathbf{v} + (\mathbf{v} \cdot \nabla) \mathbf{v} = -\nabla p + Ra\theta \boldsymbol{\lambda} + \nabla^2 \mathbf{v} + \sqrt{Ta}(\mathbf{v} \times \boldsymbol{\lambda}), \quad (1)$$

$$Pr[\partial_t\theta + (\mathbf{v} \cdot \nabla)\theta] = \nabla^2\theta + v_3, \quad (2)$$

$$\nabla \cdot \mathbf{v} = 0. \quad (3)$$

The convective flow is then governed by three dimensionless numbers: (1) Rayleigh number $Ra = g\alpha\beta d^4/(\nu\kappa)$, which is a measure of the buoyancy force, (2) Taylor number $Ta = 4\Omega^2 d^4/\nu^2$, which is proportional to the square of rotation rate, and (3) Prandtl number $Pr = \nu/\kappa$, which is the ratio of the thermal and viscous diffusive time scales. In absence of rotation ($Ta = 0$), the hydrodynamic system (equations 1-3) reduces to Spiegel's equations¹⁷ in the limit of $Pr \rightarrow 0$. The temperature field is then slaved to the vertical velocity in this limit. We consider thermally conducting and stress-free bounding surfaces. The stress-free conditions are relevant for boundaries between two fluids of large viscosity difference. They were realized in experiments by Goldstein and Graham⁴⁸. The stress-free boundary conditions are also appropriate for analytical work (e.g. amplitude equations) and constructing accurate low-dimensional models, since trigonometric eigenfunctions simplify algebra. We then have $\theta = \partial_z v_1 = \partial_z v_2 = v_3 = 0$ on the horizontal surfaces, which are located at $z = 0$ and 1 . All the convective fields are assumed to be periodic on the horizontal plane.

III. LINEAR STABILITY ANALYSIS

The linear stability results in the limit of vanishing Prandtl number may be obtained, following Chandrasekhar¹⁶, in terms of the vertical velocity v_3 . The relevant equation in the $Pr \rightarrow 0$ limit reads as:

$$\left[\nabla^2 \left\{ (\partial_t - \nabla^2)^2 \nabla^2 + Ta D^2 \right\} + Ra (\partial_t - \nabla^2) \nabla_H^2 \right] v_3(x, y, z, t) = 0, \quad (4)$$

where $D \equiv \partial_z$. The vertical velocity is expanded in normal modes, given by,

$$v_3(x, y, z, t) = W(z) \exp [i(k_x x + k_y y) + \sigma t], \quad (5)$$

where $k = \sqrt{k_x^2 + k_y^2}$ is the horizontal wavenumber. Inserting equation 5 in equation 4, and using the trial solution $W(z) = A \sin(\pi z)$, which is compatible with stress-free boundary conditions, we arrive at the following stability condition:

$$\left[(\pi^2 + k^2) \left\{ (\sigma + \pi^2 + k^2)^2 (\pi^2 + k^2) + \pi^2 Ta \right\} - k^2 Ra (\sigma + \pi^2 + k^2) \right] = 0. \quad (6)$$

The roots of the quadratic equation (6) for σ are the linear growth rates σ_{\pm} of the perturbations. They are given by,

$$\sigma_{\pm} = \frac{-2(\pi^2 + k^2)^3 + k^2 Ra \pm \sqrt{(k^2 Ra)^2 - 4\pi^2(\pi^2 + k^2)^3 Ta}}{2(\pi^2 + k^2)^2} \quad (7)$$

The two growth rates σ_+ and σ_- may either be real, or may form a complex conjugate pair.

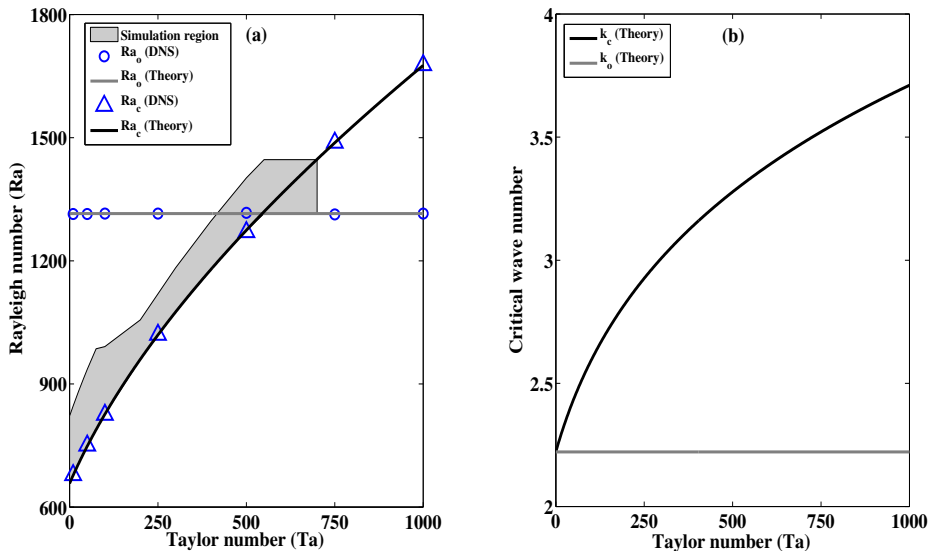


FIG. 1. Linear stability analysis in the $Pr \rightarrow 0$ limit. (a) The variation of critical Rayleigh numbers $Ra_c(Ta)$ (black curve) for the stationary convection and $Ra_o(Ta)$ (gray curve) for the oscillatory convection with Taylor number Ta . (b) The variation of critical wave numbers $k_c(Ta)$ (black curve) for the stationary convection and $k_o(Ta)$ (gray curve) for the oscillatory convection with Ta . Ra_o and k_o are independent of Ta in this limit. The symbols Δ and \circ are data obtained from DNS of full hydrodynamic system for $Ra_c(Ta)$ and Ra_o , respectively. The shaded area shows the region of the $Ra - Ta$ plane where simulations are done.

1. Stationary convection

Both the growth rates are real, if $(k^2 Ra)^2 \geq 4\pi^2(\pi^2 + k^2)^3 Ta$. Setting the larger value $\sigma_+ = 0$ yields the condition for stationary convection. The critical Rayleigh number $Ra_c(Ta)$ is given as:

$$Ra_c(Ta) = [(\pi^2 + k_c^2)^3 + \pi^2 Ta] / k_c^2, \quad (8)$$

where the critical wave number $k_c(Ta)$ satisfies the following equation:

$$2 \left(\frac{k_c^2}{\pi^2} \right)^3 + 3 \left(\frac{k_c^2}{\pi^2} \right)^2 = \left(1 + \frac{Ta}{\pi^4} \right). \quad (9)$$

Combining eqs. 9 and 8, the critical Rayleigh number $Ra_c(Ta)$ may also be written as:

$$Ra_c = 3(\pi^2 + k_c^2)^2. \quad (10)$$

The critical wavenumber, which is a real positive root of eq. 9, is:

$$k_c(Ta) = \pi \sqrt{a_+ + a_- - 1/2}, \quad a_{\pm} = \left[\frac{1}{4} \left\{ \frac{1}{2} + \frac{Ta}{\pi^4} \pm \sqrt{\left(\frac{1}{2} + \frac{Ta}{\pi^4} \right)^2 - \frac{1}{4}} \right\} \right]^{\frac{1}{3}}. \quad (11)$$

2. Oscillatory convection

The two growth rates σ_+ and σ_- form a complex conjugate pair, if $(k^2 Ra)^2 < 4\pi^2(\pi^2 + k^2)^3 Ta$. Insertion of $\sigma_{\pm} = s \pm i\omega$ in equation 7 leads to the expressions for s and ω :

$$s = \frac{-2(\pi^2 + k^2)^3 + k^2 Ra}{2(\pi^2 + k^2)^2}, \quad \omega(Ta) = \frac{\sqrt{4\pi^2(\pi^2 + k^2)^3 Ta - k^4 Ra^2}}{2(\pi^2 + k^2)^2}. \quad (12)$$

Setting $s = 0$ leads to the condition for marginal stability for oscillatory convection. The critical wavenumber k_o and the critical Rayleigh number Ra_o for the oscillatory instability in the $Pr \rightarrow 0$ limit are found to be $k_o = \pi/\sqrt{2} \approx 2.22$ and $Ra_o = 27\pi^4/2 \approx 1315$, respectively. Notice that k_o and Ra_o are independent of Ta in this limit. The angular frequency ω becomes real, if $Ta > 27\pi^4/8 \approx 328$. The convection is oscillatory at the onset if $Ra_o < Ra_c(Ta)$. This is possible for $Ta \geq 548$, and the dimensionless angular frequency at the onset of oscillatory convection for $Ta = 548$ is $\omega_o = \sqrt{\frac{2}{3} \left(548 - \frac{27\pi^4}{8} \right)} \approx 12.1$. Simulations are done for parameters of the shaded region of the $Ra - Ta$ plane [see fig. 1 (a)]. The results of linear stability analysis are summarized in figure 1. Blue triangles and circles in figure 1 (a) are values of $Ra_c(Ta)$ and Ra_o respectively, computed from DNS. The fluid patterns near onset of oscillatory convection have been investigated in detail using DNS recently³². We have therefore carried out DNS in the vicinity of the bicritical point ($Ra_c = Ra_o$) and in the stationary convective regime.

IV. DIRECT NUMERICAL SIMULATIONS

The direct numerical simulations (DNS) of the hydrodynamical system (equations 1-3) with the stress-free boundary conditions in the limit $Pr \rightarrow 0$ are carried out using the pseudo

spectral method (see, Pharasi & Kumar³² for details) using an open source code Tarang⁴⁹. All the components v_1 , v_2 and v_3 of the velocity field are expanded as:

$$v_1(x, y, z, t) = \sum_{l,m,n} U_{lmn}(t) e^{i(lk_x x + mk_y y)} \cos n\pi z, \quad (13)$$

$$v_2(x, y, z, t) = \sum_{l,m,n} V_{lmn}(t) e^{i(lk_x x + mk_y y)} \cos n\pi z, \quad (14)$$

$$v_3(x, y, z, t) = \sum_{l,m,n} W_{lmn}(t) e^{i(lk_x x + mk_y y)} \sin n\pi z. \quad (15)$$

The perturbations with the critical wavenumber $k_c(Ta)$ are the most dangerous, as soon as the Rayleigh number Ra is raised above the threshold $Ra_c(Ta)$ for convection. In addition, components with longer wavelengths (or smaller wave numbers) are always present in larger containers. We have considered a rectangular simulation box of size $(2\pi/k_x) \times (2\pi/k_y) \times 1$. We can investigate various patterns arising from the nonlinear interaction of two wave vectors \mathbf{k}_1 and \mathbf{k}_2 . The code allows various possibilities for the choice of fluid patterns. We may have $\mathbf{k}_1 = \alpha k_c \mathbf{e}_1 + \beta k_c \mathbf{e}_2$ and $\mathbf{k}_2 = \alpha k_c \mathbf{e}_1 - \beta k_c \mathbf{e}_2$ for a given choice of α and β . A nonlinear interaction of two wave vectors \mathbf{k}_1 and \mathbf{k}_2 generates a third wave vector $\mathbf{k}_3 = -[\mathbf{k}_1 + \mathbf{k}_2]$. A pattern involving \mathbf{k}_1 , \mathbf{k}_2 and \mathbf{k}_3 is excited, if they all fit in the chosen simulation box. The angle ϕ between two wave vectors \mathbf{k}_1 and \mathbf{k}_2 is then given by $\cos \phi = \mathbf{k}_1 \cdot \mathbf{k}_2 / |\mathbf{k}_1| |\mathbf{k}_2| = (\alpha^2 - \beta^2) / (\alpha^2 + \beta^2)$. The code can also investigate the interaction of two wave vectors $\mathbf{k}_1 = \alpha k_c \mathbf{e}_1$ and $\mathbf{k}_2 = \beta k_c \mathbf{e}_2$. The parameter α has been set equal to unity for most of the cases, while the parameter β has been varied. We allowed the ratio $\eta = k_x/k_y = \alpha/\beta$ to vary in the range $1/\sqrt{3} \leq \eta \leq 10$. The variation of the parameter η has facilitated the investigation of a variety of fluid patterns. For $\eta \geq 4$, we observe the replacement of a set of wavy rolls by a new set of wavy rolls of different wave numbers oriented at an angle of $\phi = \arctan(1/\eta)$ at the primary instability for all possible values of Ta . To investigate standard Küppers-Lortz patterns, we set $k_x = k_c/2$ and $k_y = \sqrt{3}k_c/2$.

The spatial grid resolutions of $64 \times 64 \times 64$ and $128 \times 128 \times 128$ have been used for DNS, which are good enough to resolve the flow structures at smaller rotation rates and smaller values of the reduced Rayleigh number $r = Ra/Ra_c(Ta)$. The time advancement is done using the standard fourth order Runge-Kutta (RK4) integration scheme. The time step δt for the integration was 0.001. We started a simulation for a given value of Ta and Ra with random initial conditions. The reduced Rayleigh number r was increased in small steps ($0.001 \leq \delta r \leq 0.1$). The final values of all the fields after long time were used as initial

conditions for the next run. We also did simulations at higher values of r and decreased it in small steps to find out any hysteresis. We did not find any hysteresis in the entire range of parameters investigated in this paper. We performed several runs of the hydrodynamic system for a range of reduced Rayleigh numbers ($1 < r \leq 1.25$) for different values of the ratio η .

The horizontal aspect ratio η of a simulation box does not necessarily mean the same of an experimental container in pseudo spectral method. The size of a rectangular simulation box fixes the lower cut-off values of the interacting wave vectors. A simulation box with square horizontal cross-section of side $L > 2\pi/k_c$ would allow interaction of two mutually perpendicular wave vectors of equal magnitude $k < k_c$. A larger experimental container with a square horizontal cross-section allows several possibilities of an interaction between two wave vectors in mutually perpendicular directions.

V. RESULTS AND DISCUSSIONS

As the Rayleigh number Ra is raised above a critical value $Ra_c(Ta)$ for a given value of Ta , the convection sets in. The fluid patterns at the instability onset depend, in general, on the Taylor number Ta and the ratio η . Chaotic patterns were observed at the primary instability in certain windows of Ta in all the simulation boxes. We observed periodic dynamics at the primary instability in smaller boxes ($\eta < 4$) for smaller values of Ta . The fluids patterns at the primary instability as computed from DNS are listed in Table I.

A. Küppers-Lortz instability: $\eta = 1/\sqrt{3}$

We now set $\alpha = 1/2$ and $\beta = \sqrt{3}/2$, which fixes the parameter $\eta = 1/\sqrt{3}$. This allows the investigation of the interaction of two rolls in mutually perpendicular directions. In addition, it also allows us to investigate the interaction of two wave vectors $\mathbf{k}_1 = \frac{k_c}{2} (-\mathbf{e}_1 + \sqrt{3}\mathbf{e}_2)$ and $\mathbf{k}_2 = -\frac{k_c}{2} (\mathbf{e}_1 + \sqrt{3}\mathbf{e}_2)$. The nonlinear interaction of two wave vectors in the latter case generates a third wave vector $\mathbf{k}_3 = k_c\mathbf{e}_1$. The three wave vectors are of equal magnitude ($|\mathbf{k}_1| = |\mathbf{k}_2| = |\mathbf{k}_3| = k_c$), and they are oriented with each other at 120° . This is the well known case of Küppers-Lortz instability^{21,22}, who considered the limit $Pr \rightarrow \infty$ in their original work with stress-free boundaries. The corresponding patterns dynamics showed

TABLE I. Convective flows computed from the direct numerical simulation just above the primary instability ($r = 1.005$) for several values of Taylor number for boxes with different aspect ratio $\eta = k/q$. We have set $k_x = k_c(Ta)$ and $r = Ra/Ra_c$ for $0 \leq Ta \leq 550$ in DNS. The flow patterns show periodic bursting (PB) as well as chaotic bursting (CB) for $\eta = 1$, periodic wavy rolls (WR) at lower values of Ta and Küppers-Lortz (KL) patterns for $Ta \geq 40$ for $\eta = 1/\sqrt{3}$, WR at smaller values of Ta and KL and generalized Küppers-Lortz (GKL) patterns for higher values of Ta for $\eta = 2$, and the KL patterns for $\eta \geq 4$, respectively. We have set $k_x = k_o$ and $r = Ra/Ra_o$ for $Ta > 550$. We observe quasiperiodic cross-rolls in oscillatory regime ($Ta > 550$) for $\eta = 1$ and 2, while KL or GKL patterns for $\eta = 1/\sqrt{3}$ and $\sqrt{3}$. The angles between the interacting rolls in the horizontal plane are also mentioned below the appropriate patterns.

α	β	$\eta = \alpha/\beta$	Fluid Patterns at different values of Ta									
			Ta =10	25	40	50	100	500	550	575	700	
1/2	$\sqrt{3}/2$	$1/\sqrt{3}$	WR	WR	KL	KL	KL	GKL	GKL	GKL	KL	
					(30.0°)	(40.8°)	(40.8°)	(60.0°)	(60.0°)	(60.0°)	(60.0°)	
								(30.0°)	(30.0°)	(30.0°)		
1	1	1	PB	CB	PB	PB	CB	CB	CB	QCR	QCR	
1	$1/\sqrt{3}$	$\sqrt{3}$	WR	WR	WR	WR	KL	KL	GKL	GKL	-	
							(30.0°)	(30.0°)	(60.0°)	(60.0°)	-	
								(30.0°)	(30.0°)			
1	1/2	2	WR	KL	KL	KL	KL	GKL	GKL	GKL	QCR	
				(26.6°)	(26.6°)	(26.6°)	(26.6°)	(26.6°)	(26.6°)	(26.6°)		
								(63.4°)	(63.4°)	(63.4°)		
1	1/4	4	KL	KL	KL	-	-	-	-	-	-	
			(14.0°)	(14.0°)	(14.0°)							
1	1/10	10	KL	KL	KL	-	-	-	-	-	-	
			(5.7°)	(5.7°)	(5.7°)							

replacement of one set of straight rolls by another of set of rolls of the same wavelength but oriented with the older set at an angle of 60°. This situation is quite different than

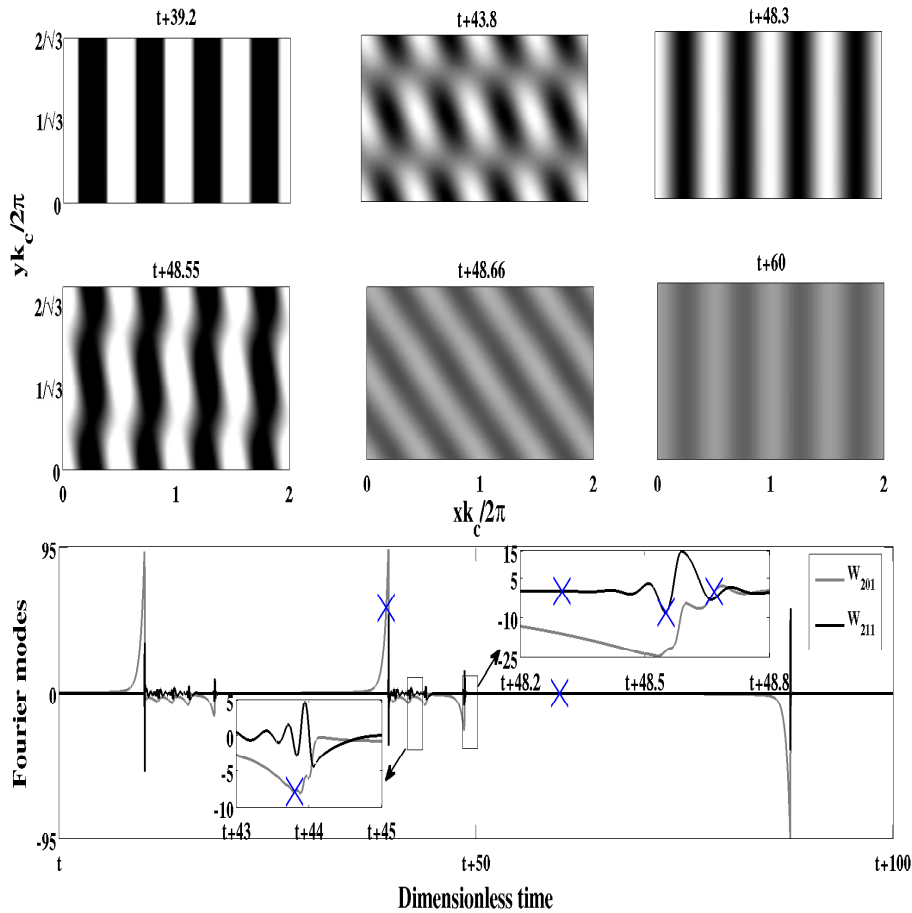


FIG. 2. Contour plots of the temperature field at $z = 0.5$ showing Küppers-Lortz instability ($\eta = 1/\sqrt{3}$) at the onset ($r = 1.005$) for $Ta = 50$. The variations of the two largest Fourier modes W_{201} and W_{211} with time are shown in the lower row. The contour plots are for the time instants marked by cross (\times) in the lower row. The intensity of the gray level in the contour plots is larger for larger value of the mode $|W_{201}|$.

choosing $\mathbf{k}_1 = k_c \mathbf{e}_1$ and $\mathbf{k}_2 = \sqrt{3}k_c \mathbf{e}_2$, which gives $\eta = 1/\sqrt{3}$. This describes an interaction of two wave vectors in mutually perpendicular directions: one with wave number equal to k_c another with wavenumber equal to $\sqrt{3}k_c$. We have listed the values of α and β in the first two columns of Table I.

The replacement of a set of rolls by a new set of rolls of the same wavelength and inclined at an angle of ϕ with the old set of rolls is well known as Küppers-Lortz (KL) patterns. We observed in some cases that the wavelength of the new set of rolls was different from

that of the old set. We have termed these patterns also as KL patterns here. The angle ϕ between two sets of rolls depends on the interacting wave vectors. We have also observed a new possibility. The first set of rolls is replaced by a second set of rolls oriented at an angle ϕ with the first, and then the second set of rolls is replaced by a third set of rolls oriented at an angle $90^\circ - \phi$ with second set. This involves a competition of three sets of rolls of different wavelengths. These patterns are termed here as generalized Küppers-Lortz (GKL) patterns.

Clune and Knobloch⁵⁰ investigated fluid patterns in rotating RBC using amplitude equations and found the possibility of standing waves at the instability onset at smaller rotation rates for $Pr < 0.442$ with no-slip boundary conditions. They showed that the critical value Ta_{KL} of the Taylor number for KL instability and the angle ϕ between two sets of oblique rolls of the same wavelengths at the onset of KL instability become smaller, as Pr is decreased. They also predicted small angle instability for stress-free boundaries in case of a high Prandtl number fluid ($Pr = 100$). The angle between two wave vectors $\mathbf{k}_1 = \alpha k_c \mathbf{e}_1 + \beta k_c \mathbf{e}_2$ and $\mathbf{k}_2 = \alpha k_c \mathbf{e}_1 - \beta k_c \mathbf{e}_2$ of the same magnitude k_c would lead to small angle instability if $\alpha^2 + \beta^2$ and $\alpha^2 - \beta^2$ simultaneously tend to unity, which is not possible. The small angle instability involving two sets of rolls of the critical wavelength λ_c is unlikely to occur unless $\beta \rightarrow 0$. The small angle instability, however, with any two wave vectors is possible in two cases: (i) α remains finite and $\beta \rightarrow 0$ or (ii) $\alpha \rightarrow 0$ and $\beta \rightarrow 0$. We do observe the angle ϕ decreasing as η increases in the first case but there is no divergence observed in DNS for $\eta \leq 10$. Clune and Knobloch also mentioned that some of their conclusions were valid for $Pr \sim O(1)$, and they would require modification in the limit of $Pr \rightarrow 0$.

Cox and Mathews²⁷ investigated the instability of a set of straight rolls to a new set of similar rolls inclined at a small angle with the old set in case of stress-free boundary conditions using amplitude equations for $Pr \gg 1$. They predicted a system of rolls is always unstable to a new set of rolls at infinitesimal angle ($\phi \rightarrow 0$), if $Ta \geq Ta_c = 4\pi^4$. However, Cox and Mathews considered only those modes for the vertical vorticity, which are independent of the vertical coordinates. This approach does not consider all possible nonlinear interactions. For example, the vorticity mode Z_{211} (Z_{121}) interacts nonlinearly with the velocity mode W_{101} (W_{011}) and generates other vorticity modes: Z_{110} , Z_{112} , Z_{310} (Z_{130}) and Z_{312} (Z_{312}). Similarly, the interaction of the vorticity mode Z_{110} with the 2D roll mode W_{101} (W_{011}) not only contributes to another 2D roll mode W_{011} (W_{101}) but also

generates higher velocity modes: W_{111} , and W_{211} (W_{121}). We have observed that the maxima of $|Z_{121}|$ and $|Z_{211}|$ are larger than the maxima of $|Z_{110}|$ in a finite size periodic simulation box, although the linear decay rate of the mode Z_{110} is much smaller than the linear decay rates of the modes Z_{211} and Z_{121} . The infinitesimal angle instability in a small or narrow simulation box ($\eta \leq 10$) is unlikely at least near onset. We have not found this instability for rectangular container with $\eta \leq 2$ (please see patterns for $Ta \geq 500$ listed in Table I). Any experimental container has a typical length scale in the horizontal plane, which restricts the maximum wavelength of the perturbations. Similarly, any periodic simulation box used in DNS using pseudo spectral method has a finite size. This imposes a maximum limit on the possible wavelength of perturbations. This is independent of the fact whether one uses free-slip or no-slip boundaries on the top and bottom surfaces. Although long wavelength perturbations are easily excited with free-slip boundaries, there is a maximum cut-off value in practice. Square patterns were observed in experiments with CO_2 ($Pr = 0.93$) and argon ($Pr = 0.69$) gases in a cylindrical container⁴⁴. In addition, the bursting of patterns was not found in earlier studies^{27,50} as observed in experiments by Bajaj et al⁴⁵. We have carried out DNS for the limiting case of $Pr \rightarrow 0$. The primary instability even without rotation is quite complex in very low-Prandtl-number fluids ($Pr \ll 1$) with stress-free boundaries^{14,15}. We have chosen one side of the rectangular simulation box of a variable length and the ratio $\eta = k_y/k_x$ is varied between $1/\sqrt{3}$ and 10. Periodic simulation boxes with narrow rectangular cross-section or smaller square cross-section in the horizontal plane do not allow two sets of rolls at infinitesimal inclination.

Various convective patterns computed from DNS for $\eta = 1/\sqrt{3}$ at different values of Ta are summarized in Table I. The angle between the two sets of inclined rolls for KL or GKL patterns are mentioned in the brackets. A listing of two angles mean that old set of rolls may be replaced by a new sets inclined at any of the two values mentioned. We observed periodic wavy rolls at the primary instability for $Ta < 40$. KL instability is observed for $40 \leq Ta \leq 100$ and again for $Ta = 700$, while GKL patterns are observed for $500 \leq Ta \leq 575$. GKL patterns are observed near the bicritical point. Figure 2 shows contour plots of the temperature fields at $z = 0.5$ just above the onset of convection ($r = 1.005$) at six different instants for $Ta = 50$. The fluid patterns consist of straight rolls, wavy rolls and oblique rolls, which appear irregularly in time. The temporal variations of the two largest Fourier modes W_{201} (gray curve) and W_{211} (black curve) corresponding to this

sequence of patterns are displayed in the lower row of figure 2. The temporal variation of the leading modes shows unsteady convection at the primary instability. The contour plots are for the time instants marked by blue crosses in the third row of figure 2. Occasionally, one set of rolls are replaced by a new set of oblique rolls of the same wavelengths. However, there is a difference from KL instability for $Pr \gg 1$. The leading Fourier mode W_{201} describing a set of straight rolls keeps growing almost exponentially until it crosses a critical value. The wavy mode W_{211} is then excited, and the straight rolls become wavy. Standing waves are generated along the roll axis. The generation of waves along the roll axis transfers the energy from the poloidal flow fields to the toroidal flow fields. The transferred energy dissipates quickly in viscous fluids. As a consequence, the magnitude of W_{201} decreases sharply to a very small value. The waves along the rolls disappear a little later. The mode W_{201} again starts growing and the waves are generated only when roll intensity crosses a critical value. When W_{211} is comparable to W_{201} , the straight or wavy rolls are replaced by a new set of rolls oriented at an angle $\phi \approx 40^\circ$. The bursting of patterns has been observed in experiments by Bajaj et al⁴⁵. The variation of the amplitude of the roll modes also showed critical bursting. This kind of behaviour is also observed in a low-dimensional model of convection in very low-Prandtl-number fluids¹⁹. The phenomenon of critical bursting is known to occur in the spring-block model⁵¹. KL instability shows the features of the critical bursting in the limit $Pr \rightarrow 0$.

B. Patterns in a small square box: $\eta = 1$

The fluid patterns are quite different in a simulation box with a square horizontal cross-section ($\eta = 1$). The simulations show a competition between two sets of mutually perpendicular straight rolls at the primary instability. The dynamics may be periodic or chaotic depending upon the value of Ta . The evolution of convective patterns with time is displayed in the first and second rows of figure 3 for $r = 1.001$ and $Ta = 10$. Patterns are displayed at eight equally spaced instants during one period (τ) of oscillation. The patterns consist of a set of straight rolls either parallel to the x axis or parallel to the y axis for more than two-thirds of the oscillation period. The change in orientation of rolls occurs within a very short period. The temporal variation of the leading Fourier modes W_{101} (black curve) and W_{011} (gray curve) for these patterns is shown in the third row of figure 3 for one oscillation

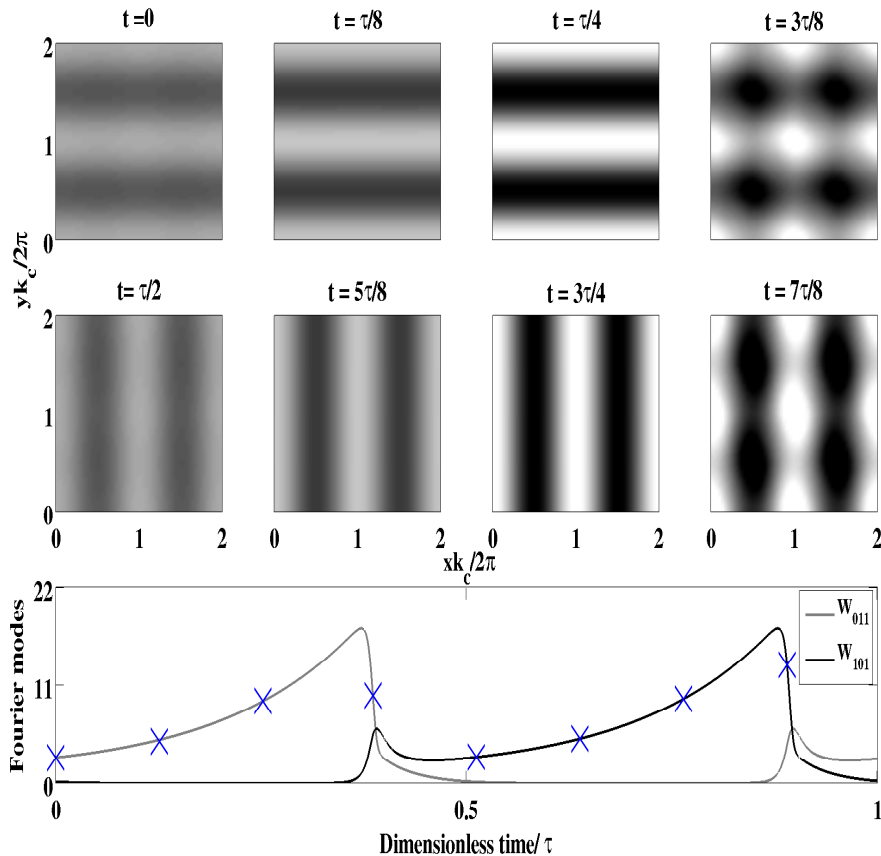


FIG. 3. Periodic competition of two sets of mutually perpendicular straight rolls for $r = 1.001$ and $Ta = 10$, as obtained from DNS in a small square box [$k_x = k_y = k_c(Ta)$, $\eta = 1$]. The mid-plane ($z = 0.5$) contour plots of the temperature field are shown at eight equally spaced instants during the oscillation period ($\tau = 12.74$) in the first two rows. The black (white) regions in the contour plot correspond to relatively cooler (warmer) fluid. The third row displays the temporal variation of the two largest modes W_{101} (black curve) and W_{011} (gray curve).

period. The Fourier mode W_{011} grows exponentially with time, while the other mode W_{101} decays to zero. The mode W_{101} is excited from its zero value when the growing W_{011} exceeds a critical value, which is slightly less than its maximum value. This stops further growth of the rolls parallel to the x axis. The mode W_{011} starts decaying sharply, while the mode W_{101} keeps growing. We observe square patterns when $|W_{011}| = |W_{101}|$ and cross-rolls for $|W_{011}| \neq |W_{101}|$. These cross-rolls are also known as asymmetric squares, as $k_x = k_y = k_c$. In a very short period, the rolls parallel to the x axis disappear. We then observe rolls growing parallel to the y axis. A set of rolls parallel to the x axis is once again excited, as soon as the

fluid velocity in the set of rolls parallel to the y - axis exceeds a large ($\gg 1$) critical value. This is also an example of critical bursting of rolls. Patterns show periodic bursts (PB) as well as chaotic bursts (CB) as Ta is varied. The period of exponential growth of any set of rolls to a critical value is much larger than the period of bursting. The phenomenon of bursting reported here is an example of non-local bifurcation at the instability onset. This behaviour cannot be captured in an analysis based on local bifurcation theory around the conduction state or a stationary convective state. These patterns were not reported before at the instability onset in a rotating RBC. They are qualitatively new and more likely to occur in a square container. The Fourier modes W_{101} and W_{011} show relaxation oscillation due to the presence of two time scales. Their temporal evolution of these modes have strong resemblance with the time series recorded by Bajaj et al.⁴⁵ leading to bursting of patterns.

The temporal evolutions of the two largest Fourier modes W_{101} (blue curves) and W_{011} (pink curves) slightly above the onset of convection ($r = 1.001$) are shown in figure 4 for $\eta = 1$ at different values of Ta . In the absence of rotation ($Ta = 0$), the solution is always chaotic at the onset^{13,14} in the limit $Pr \rightarrow 0$ [see figure 4 (a)]. The two largest Fourier modes W_{101} and W_{011} vary chaotically in time except in narrow windows of Ta near $Ta = 10$ and $Ta = 40$. Figure 5 shows the phase portraits of the flow dynamics in the $W_{101} - W_{011}$ plane corresponding to the temporal evolution of the Fourier modes given in Figure 4. Unsteady solutions in the different quadrants of the $W_{101} - W_{011}$ plane get entangled at the onset for $Ta = 0$ [see figure 5 (a)]. The glued periodic and chaotic solutions are observed only in one of the four quadrants of the $W_{101} - W_{011}$ plane for $Ta \neq 0$ [see figure 5 (b)-(i)]. A glued limit cycle at smaller values of Ta become chaotic as Ta is raised. The chaotic glued oscillation breaks into two sets of distinct solutions with further increase in Ta . Figure 5 (d), (e) and (f) show two distinct sets of period-four, period-two and period-one limit cycles at $Ta = 28$, 30 and 40 respectively. The fluid patterns appeared as cross-rolls due to the competition between two sets of parallel rolls in mutually perpendicular directions. The competition was found to be periodic as well as chaotic with the variation of Ta . A transition from chaotic cross-rolls to chaotic rolls was observed for larger values of Ta [see figure 4 (i)]. The temporal variations of both the Fourier modes show critical bursting. The bifurcation at the primary instability is nonlocal for $Ta \leq 100$. The second row of Table I lists various possible fluid patterns computed from DNS for $\eta = 1$.

Various Fluid patterns, computed from DNS for different regions of the parameter space

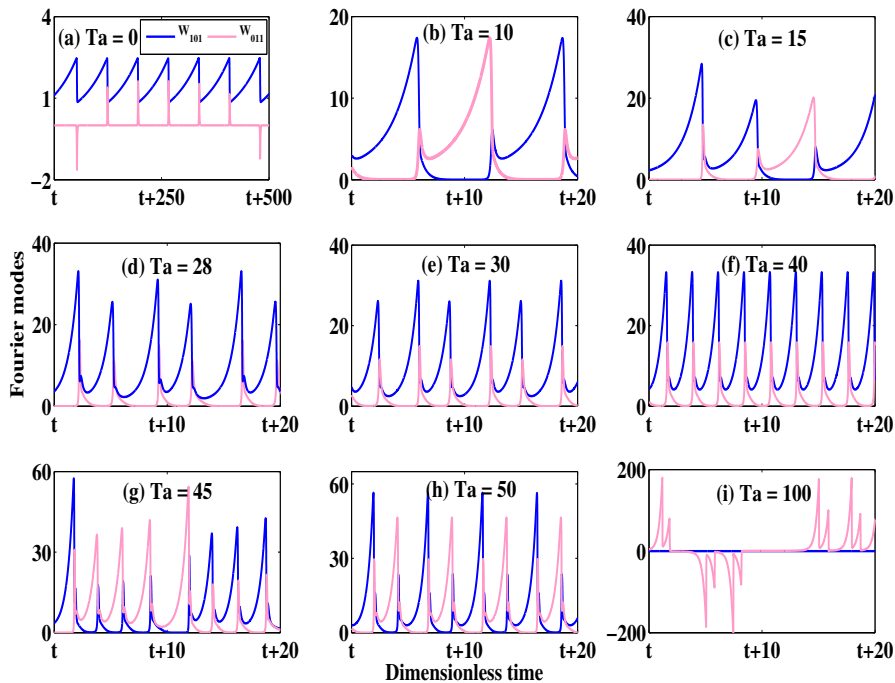


FIG. 4. Temporal variation of the two largest Fourier modes W_{101} (blue curves) and W_{011} (pink curves) near primary instability ($r = 1.001$) for different values of Ta for $\eta = 1$. As soon as the mode W_{101} (W_{011}) reaches a critical value, the mode W_{011} (W_{101}) gets excited. The mode W_{101} (W_{011}) decays very sharply to zero, while the other mode keeps growing. For $Ta < 20$, both the modes alternately decay to zero. For $Ta > 20$, one of the modes decays to zero while the other mode falls to a finite small value. Both sets of rolls show the phenomenon of critical bursting.

$r - Ta$, are plotted in figure 6 for $\eta = 1$. Two sets of straight rolls are found to alternate at the primary instability in a square box. The dynamics is observed to be periodic (PB) for $2 \leq Ta \leq 10$ (shaded regions in figure 6) and $28 \leq Ta \leq 40$, while it is found to be chaotic (CB) for $10 < Ta < 28$. The two regimes are found to alternate as Ta is increased further. The primary instability becomes chaotic for $Ta > 55$. Boundaries of regions in the $r - Ta$ plane separating different convective patterns are marked by different symbols. The boundary of the PB and the CB patterns is marked by ‘ \triangle ’ in figure 6. As the reduced Rayleigh number r is raised for a fixed value of Ta (< 40), the minimum of the mode W_{101} or W_{011} becomes finite. We then observe a competition between straight rolls and cross-rolls. The minima of both the rolls become finite with further increase in r , and the

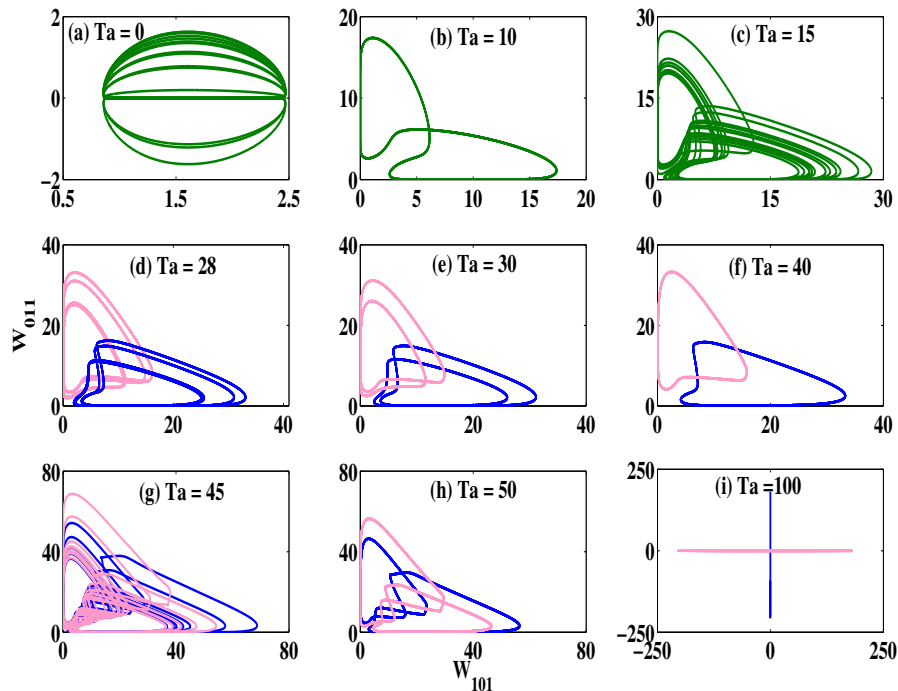


FIG. 5. The projection of the phase portraits on the $W_{101} - W_{011}$ plane near the primary instability ($r = 1.001$) for different values of Ta ($\eta = 1$). Two sets of possible phase plots (blue and pink curves) are possible in each quadrant of the $W_{101} - W_{011}$ plane. The green curves show the glued solutions. The temporal variation of these modes are given in figure 4.

corresponding patterns are oscillatory cross-rolls. We observe two possibilities: (i) two sets of rolls have equal amplitude but a phase difference between them. They appear as square patterns only for certain instants when $W_{011}(t) = \pm W_{101}(t)$, and as cross-rolls otherwise. They represent a periodic competition between two sets of oscillating cross-rolls. We have labeled them as OCR-I patterns. (ii) Two sets of rolls have unequal amplitudes. As two different solutions are possible ($|W_{101}| > |W_{011}|$ or $|W_{101}| < |W_{011}|$), we have labeled them as OCR-II. The boundary separating CB patterns from OCR-I patterns is marked by ‘ \diamond ’, and that separating OCR-I and OCR-II is marked by ‘ \star ’. If r is raised above the boundary marked by ‘ \circ ’, we observe a transition from oscillating cross-rolls (OCR-II) to stationary cross rolls (CR) via an inverse Hopf bifurcation. The range of r for which we observe stationary cross-rolls decreases with increasing Ta . We also observe two sets of stationary cross-rolls corresponding to two sets of oscillating cross-rolls. Raising r above the boundary

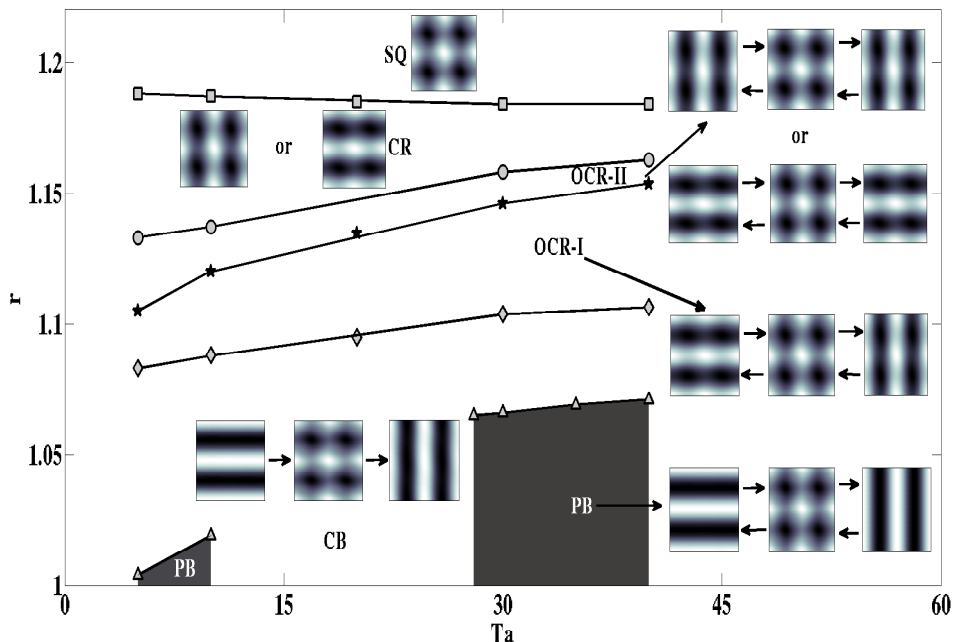


FIG. 6. Regions of various flow patterns in the $r - Ta$ plane as obtained from DNS: The boundary of periodic bursts (PB) and chaotic bursts (CB) of two sets of rolls is marked by ‘ Δ ’, while that of CB solutions and a glued oscillation of two sets of cross-rolls (OCR-I) is marked by ‘ \diamond ’. The boundary of two types of oscillatory cross-rolls (OCR-I & OCR-II) is marked by ‘ \star ’, while that of the OCR-II and the stationary cross rolls (CR) is marked by ‘ \circ ’. The square (SQ) patterns are observed above the boundary marked by ‘ \square ’. The primary instability is periodic in windows of Taylor number $2 \leq Ta \leq 10$ and $28 \leq Ta \leq 40$, but chaotic for $10 < Ta < 28$. The corresponding patterns are shown in the inset of the diagram.

marked by ‘ \square ’ leads to a regime where the stationary square patterns are observed. The transition from two sets of stationary cross-rolls to stationary square patterns occurs via a backward pitchfork bifurcation. We observed stationary square patterns at moderate rotation rates for $r \geq 1.19$. Bajaj et al⁴⁴ observed square patterns in a cylindrical container ($\eta = 1$) at higher rotation rates in water ($Pr = 5.4$) at $r = 1.09$ and in argon ($Pr = 0.69$) at $r = 1.04$.

Table II lists the various flow patterns for different values r at three different rotation rates ($Ta = 5, 10$ and 30). The patterns labeled as PB and CB cannot be captured in a

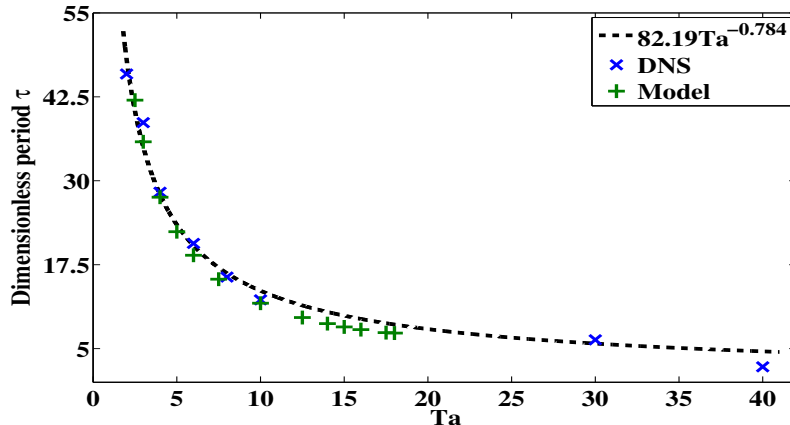


FIG. 7. Variation of the dimensionless time period τ of self-tuned oscillation (PB) at primary instability ($r = 1.001$) as a function of Taylor number Ta . The time period τ increases with decreasing Taylor number Ta . The best fit (the dashed curve) to the data obtained by DNS (marked as ‘ \times ’) for $2 < Ta \leq 40$ shows $\tau \sim Ta^{-0.784}$. The values of τ computed from the model (shown by the symbol ‘+’) agree well with those computed from DNS.

local analysis around the conduction state. The instabilities leading to PB and CB states are therefore non-local. The variation of dimensionless time period τ of the periodic bursting (PB) as a function of Taylor number Ta is shown in figure 7. The points marked by ‘ \times ’ are computed from the DNS. The points marked by ‘+’ are obtained from a model to be introduced in the next section. The time period τ of PB increases monotonically with decreasing Taylor number Ta for $2 < Ta \leq 40$. The convective dynamics is chaotic for $Ta \leq 2$, and is discussed in detail in Sec. VII.

C. Patterns in larger boxes: $\eta \geq 2$

The convective patterns in a rectangular box ($\eta = 2$) are shown in figure 8. The contour plots of the temperature field at $z = 0.5$ for three time instants are displayed in the upper row. The fluid patterns are time-periodic wavy rolls. The lower row of figure 8 shows the temporal variations of four velocity modes: W_{101} (solid black curve), W_{011} (dotted black curve), W_{111} (dashed black curve), and W_{121} (solid gray curve). The mode W_{011} always remains zero. The other three modes vary periodically in time. The modes W_{101} and W_{121} have the same temporal period, but a small phase difference. The time period of the mode

TABLE II. Flow patterns for different values of the reduced Rayleigh number r and the Taylor number Ta observed in a simulation box with $\eta = 1$. The patterns are: periodic bursting (PB), chaotic bursting (CB), oscillating cross-rolls (OCR-I, $|W_{101}|_{max} = |W_{011}|_{max}$) but with a finite phase difference between them, oscillating cross-rolls (OCR-II, $|W_{101}|_{max} \neq |W_{011}|_{max}$), stationary cross-rolls (CR) and stationary squares (SQ).

Fluid patterns	r($Ta = 5$)	r($Ta = 10$)		r($Ta = 30$)
	DNS	DNS	Model	DNS
PB	1.001 - 1.003	1.001 - 1.018	1.001 - 1.05	1.001 - 1.065
CB	1.004 - 1.082	1.019 - 1.088	-	1.066 - 1.103
OCR-I	1.083 - 1.105	1.089 - 1.120	1.051 - 1.137	1.104 - 1.146
OCR-II	1.106 - 1.132	1.121 - 1.137	1.137 - 1.157	1.147 - 1.158
CR	1.133 - 1.188	1.138 - 1.187	1.158 - 1.194	1.159 - 1.184
SQ	≤ 1.189	1.188 - 1.250	1.195 - 1.250	1.185 - 1.250

W_{111} is twice that of W_{101} . The 2D roll mode W_{101} and the nonlinear mode W_{121} have non-zero mean, but $|W_{101}| > |W_{121}|$. The nonlinear mode W_{111} has zero mean. The convective patterns are periodic standing waves along the roll-axis. We have labeled these patterns as wavy rolls (WR). Whenever $W_{111} = 0$ and $|W_{101}| \gg |W_{121}|$, the patterns appear as almost 2D rolls. The sequence of patterns is quite different from those observed for $\eta = 1$ and does not involve any critical amplitude of a set of growing rolls to trigger waves along the rolls.

The temporal evolution of convective patterns near the primary instability ($r = 1.005$) in a larger simulation box ($\eta = 4$) for $Ta = 10$, as obtained from DNS, is displayed in figure 9. The contour plots of the temperature field θ at $z = 0.5$ are shown in the upper row. The convective patterns consist of straight (2D) rolls, wavy rolls and oblique wavy rolls. Straight rolls with different intensities are observed for most of the time. The flat surface at $t = 84.5$ represents the state after bursting of rolls. Three-dimensional (3D) patterns appear only for a very short period. The temporal variations of the two largest velocity modes W_{101} (black curve) and W_{121} (gray curve) for this sequence of patterns are shown in the lower row of figure 9. Both modes vary chaotically with time. The least absolute value of the mode W_{101} is very small ($\sim 10^{-2}$), while that for the mode W_{121} is almost zero. The 2D roll mode W_{101}

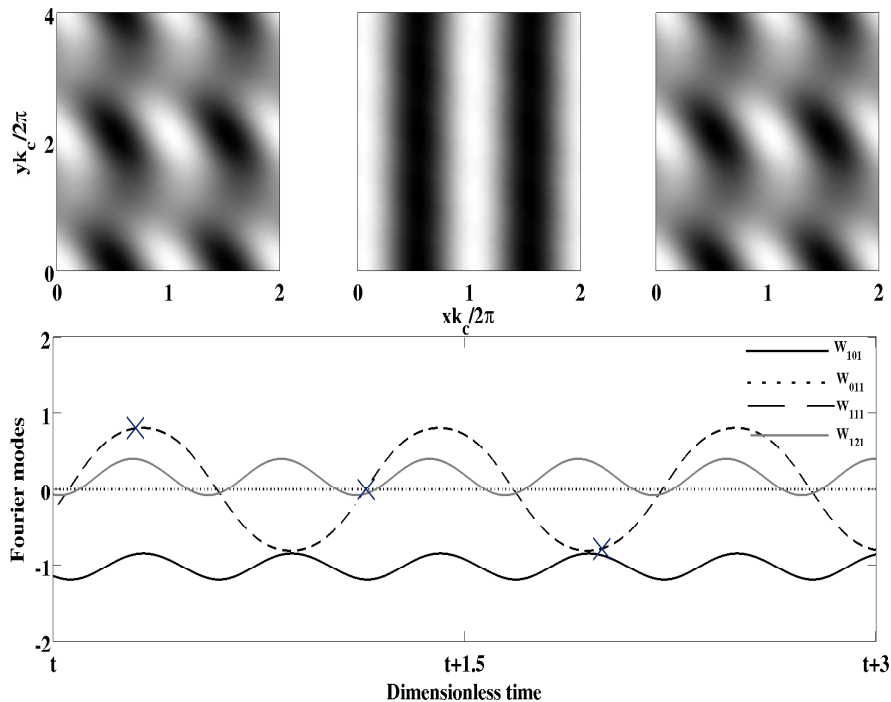


FIG. 8. Contour plots of the temperature field, computed from DNS for $z = 0.5$, $Ta = 10$ and $r = 1.005$ in a rectangular periodic box ($\eta = 2$) for three time instants are shown in the upper row. The temporal variation for Fourier modes W_{101} (solid black curve), W_{011} (dotted black curve), W_{111} (dashed black curve), and W_{121} (solid gray curve) are displayed in the lower row. The convective patterns (left to right) are computed at time instants marked by ‘ \times ’ (left to right) in the lower row. The plots show a periodic competition between wavy and straight rolls.

initially grows exponentially as predicted by the linear theory, while the nonlinear mode W_{121} remains practically zero. As soon as W_{101} exceeds a large critical value, the nonlinear mode W_{121} gets excited, as in the case of $\eta = 1$ and $1/\sqrt{3}$. We observed GKL patterns for $\eta \geq 4$. The oblique wavy rolls appear due to the generation of the wavy modes (e.g. W_{121}), which are expected in low-Prandtl-number fluids. The angle ϕ between the axis of straight rolls and that of the oblique rolls is equal to 14° in this case. For larger simulation boxes ($2 < \eta \leq 10$), the qualitative behaviour is similar. The angle ϕ , given by the relation $\phi = \arctan(k_x/k_y) = \arctan(1/\eta)$, decreases as η increases. As $\eta \rightarrow \infty$ (i.e., $k_y \rightarrow 0$), the angle $\phi \rightarrow 0$. DNS with stress-free boundaries on a periodic rectangular lattice with $\eta \leq 10$ rules out the divergence due to small angle instability. Oblique rolls and a chaotic

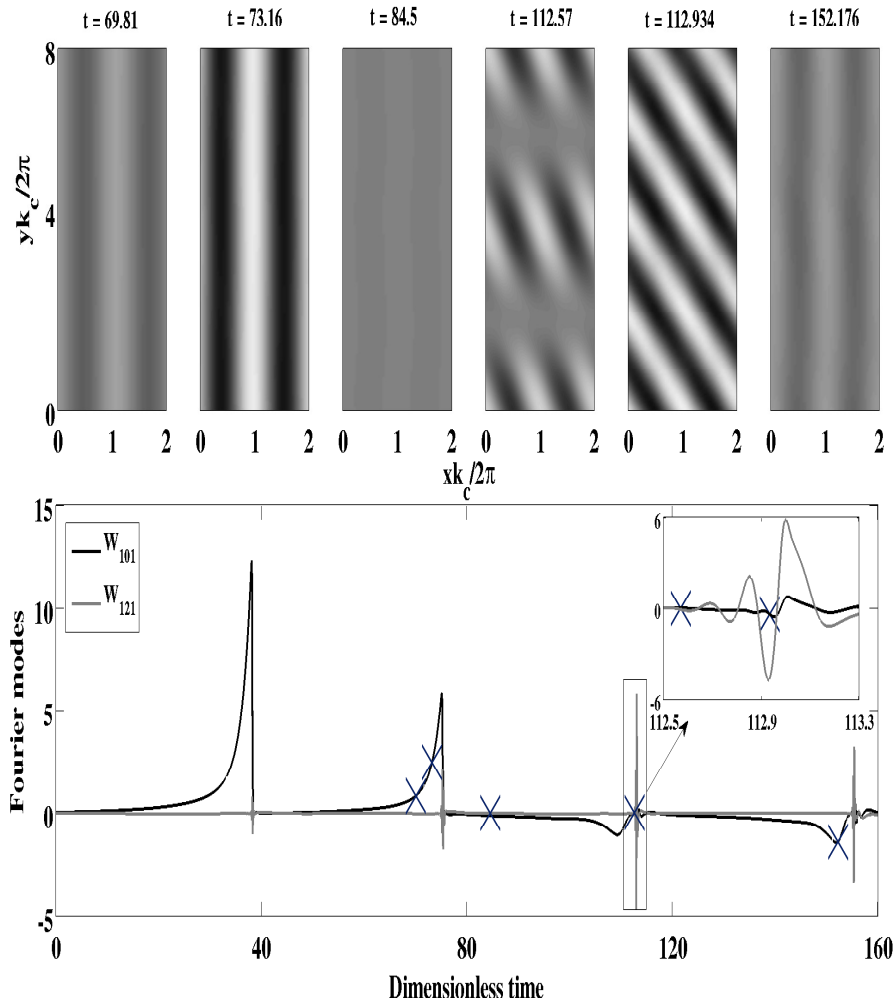


FIG. 9. Chaotic competition between two sets of rolls inclined at an angle of $\phi = 14^\circ$ for $\eta = 4$ and $Ta = 10$ just above the onset ($r = 1.005$) of convection. The upper row shows the contour plots of temperature field at $z = 0.5$. The temporal variation of two large-scale Fourier modes W_{101} (black curve) and W_{121} (gray curve) is plotted in the lower row. Six contour plots are computed at time instants marked by ‘ \times ’ on the curve shown in the lower row.

competition between two sets of mutually perpendicular rolls were observed in DNS²⁶ for rotating convection with no-slip boundary conditions.

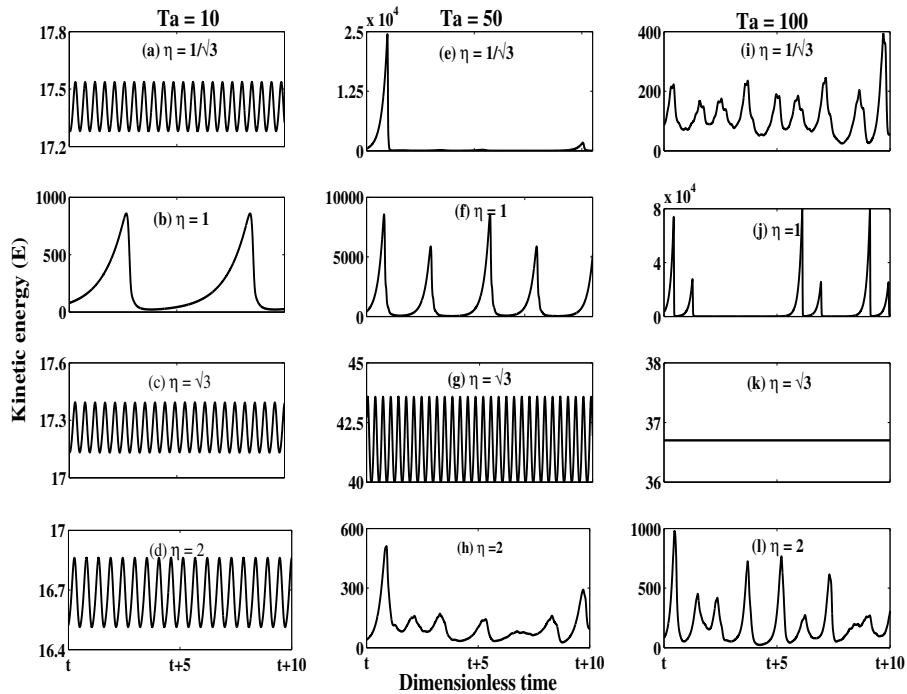


FIG. 10. Temporal variation of the boxed averaged kinetic energy (E) for different values of η and Ta near the onset of convection ($r = 1.005$).

D. Kinetic energy of fluid patterns

Figure 10 displays a comparison of the spatially averaged kinetic energy E of different patterns near onset ($r = 1.005$) for four different values of the horizontal aspect ratio and three different values of the rotation rate. The comparison of E for different values of η for $Ta = 10$ is given in the first column. Although all the patterns are time periodic, the kinetic energy for $\eta = 1$ is 50 times more than for other values of η . For $Ta = 50$ (the second column), the convection is always chaotic except $\eta = \sqrt{3}$. The maximum kinetic energy is observed for KL patterns, but PB yields maximum value of the time and space averaged kinetic energy \bar{E} . For $Ta = 100$ (the third column), the energy is higher for CB patterns than GKL and KL patterns. For a given value of η , E at the primary instability increases with the rotation rate. In addition, the convection is likely to be chaotic at the onset in very small-Prandtl-number fluids at moderate and high values of Ta .

VI. MODEL-I: A LOW DIMENSIONAL MODEL FOR $\eta = 1$

Direct numerical simulations are hugely time consuming for computing the bifurcation diagram. Amplitude equations^{27,28,55} are usually constructed in the case of a local bifurcation to save time and understand unfolding of bifurcations better. Amplitude equations assuming local bifurcations at the primary instability may not be suitable to capture the fluid patterns in zero-Prandtl-number convection with rotation. We therefore construct a low-dimensional dynamical system to capture the sequence of bifurcations in zero-Prandtl-number convection with rotation. We first eliminate the pressure term from hydrodynamic equations by applying curl ($\nabla \times$) once to Eq 1. This leads to an equation for the vorticity $\boldsymbol{\omega} = \nabla \times \mathbf{v}$, whose vertical component ω_3 is given by,

$$\partial_t \omega_3 = \nabla^2 \omega_3 + \sqrt{Ta} \partial_z v_3 + [(\boldsymbol{\omega} \cdot \nabla) v_3 - (\mathbf{v} \cdot \nabla) \omega_3]. \quad (16)$$

Operating by curl twice ($\nabla \times \nabla \times$) on Eq 1 and using Eq 3 leads to an equation for the vertical velocity v_3 given as:

$$\partial_t (\nabla^2 v_3) = \nabla^4 v_3 + Ra \nabla_H^2 \theta - \sqrt{Ta} \partial_z \omega_3 - \boldsymbol{\lambda} \cdot \nabla \times [(\boldsymbol{\omega} \cdot \nabla) \mathbf{v} - (\mathbf{v} \cdot \nabla) \boldsymbol{\omega}], \quad (17)$$

We expand $v_3(x, y, z, t)$ and $\omega_3(x, y, z, t)$ in the Fourier modes as:

$$v_3 = \sum_{l,m,n} [\tilde{W}_{lmn}(t) \cos lkx \cos mky + \tilde{W}_{\bar{l}\bar{m}n}(t) \sin lkx \sin mky] \sin n\pi z, \quad (18)$$

$$\omega_3 = \sum_{l,m,n} [\tilde{Z}_{lmn}(t) \cos lkx \cos mky + \tilde{Z}_{\bar{l}\bar{m}n}(t) \sin lkx \sin mky] \cos n\pi z. \quad (19)$$

We set $k = k_c(Ta)$ in the model, as is done in DNS. The horizontal velocities v_1, v_2 and the horizontal vorticities ω_1, ω_2 may be computed using the divergence-free nature of the velocity \mathbf{v} and vorticity $\boldsymbol{\omega}$ fields using the expansions given in Eqs. 18-19. We start with the marginal modes determined by the linear theory¹⁶ and add higher-order modes generated due to the nonlinear interaction of the linear and nonlinear modes. We select eight large-scale modes for the vertical velocity v_3 : $\tilde{W}_{101}, \tilde{W}_{011}, \tilde{W}_{112}, \tilde{W}_{\bar{1}\bar{1}2}, \tilde{W}_{211}, \tilde{W}_{2\bar{1}1}, \tilde{W}_{121}, \tilde{W}_{\bar{1}\bar{2}1}$, and twelve real modes for the vertical vorticity ω_3 : $\tilde{Z}_{101}, \tilde{Z}_{011}, \tilde{Z}_{112}, \tilde{Z}_{\bar{1}\bar{1}2}, \tilde{Z}_{211}, \tilde{Z}_{2\bar{1}1}, \tilde{Z}_{121}, \tilde{Z}_{\bar{1}\bar{2}1}, \tilde{Z}_{\bar{1}\bar{1}0}, \tilde{Z}_{200}, \tilde{Z}_{020},$ and $\tilde{Z}_{2\bar{2}0}$. Notice that the vertical vorticity has two types of modes: \tilde{Z}_{lm0} and \tilde{Z}_{lmn} . The first set of modes do not depend on the z coordinates, while the second

set of modes depend on the z coordinate. Any conclusions without considering both types of modes may not represent nonlinear behaviour correctly. Those vertical vorticity modes which couple linearly with the vertical velocity modes would play significant roles at higher rotation rates, and they should also be considered in a model suitable at higher values of Ta . Projecting the hydrodynamic system (Eqs 16-17) on these modes, we get a dynamical system consisting of twenty modes. This is done using the software ‘MAPLE’. This model, called as model I, is then integrated using standard $RK4$ integration scheme. The model shows good qualitative agreement with DNS for low values of the Taylor number ($2 \leq Ta \leq 15$). For lower values of Ta , the model captures all the instabilities observed in DNS over a wide range of reduced Rayleigh number r ($1 < r \leq 1.25$) except for the chaotic behavior observed in the DNS. The comparison of the results computed from the model with those obtained from DNS for $Ta = 10$ are listed in table II.

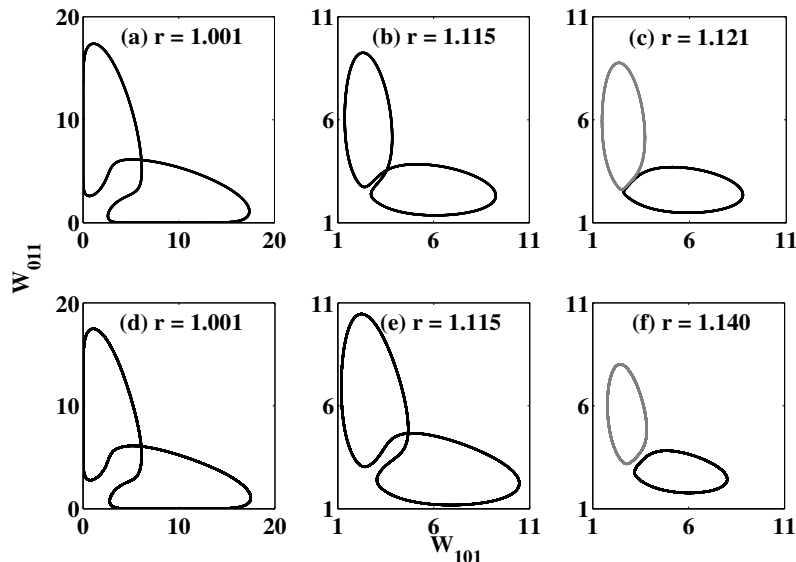


FIG. 11. Phase portraits for $Ta = 10$ and the aspect ratio $\eta = 1$ for different values of r . The upper row displays the results computed from DNS for (a) $r = 1.001$, (b) $r = 1.115$, and (c) $r = 1.121$. The lower row shows the results obtained from the model for (d) $r = 1.001$, (e) $r = 1.115$, and (f) $r = 1.140$. The results obtained from the model are in good agreement with those computed from DNS.

A. The model with $L = \lambda_c$

We now compare the results of the model for a square horizontal cross-section of each side $L = \lambda_c = 2\pi/k_c(Ta)$ with those obtained from DNS for $Ta = 10$. Figure 11 displays the periodic dynamics of the system near the instability onset for $Ta = 10$ in the $W_{101} - W_{011}$ plane. The limit cycles in the upper row [11(a)-(c)], computed from DNS, describe periodic dynamics for different values of r . The limit cycles in the lower row [11(d)-(f)] are obtained from the model. The limit cycle in figure 11(a) corresponds to PB patterns shown in figure 3 just above the instability onset ($r = 1.001$). Parts of the limit cycle lie on the W_{101} and W_{011} axes. We observe straight rolls parallel to the x (y) axis for the period $W_{011} = 0$ ($W_{101} = 0$). The limit cycle computed from the model for the same parameter value is shown in figure 11(d). They are in very good agreement. The variation of the period τ of the PB patterns near the instability onset with Ta , obtained from the model, is shown by ‘+’ mark in figure 7. The period τ computed from DNS agrees well with that obtained from the model.

As r is raised in small steps, keeping Ta fixed, we observe secondary bifurcations. Figure 11(b) shows a limit cycle, obtained from DNS, for $r = 1.115$. Here $|W_{101}|_{max} = |W_{011}|_{max}$ and $|W_{101}|_{min} = |W_{011}|_{min} \neq 0$. They describe OCR-I patterns. The trajectory forming the limit cycle appears to intersect each other because we have shown the projection of higher (64^3) dimensional phase space on the $W_{101} - W_{011}$ plane. With further increase in r , the limit cycle corresponding to OCR-I patterns breaks into two smaller limit cycles. Figure 11(c) displays two smaller limit cycles at $r = 1.121$. The smaller limit cycles with $|W_{011}|_{max} \neq |W_{101}|_{max}$ describe two possible states of OCR-II patterns. The model also shows a larger limit cycle (OCR-I patterns) for $r = 1.115$ [see, figure 11(e)], which breaks into one of the two possible smaller limit cycles [figure 11(f)] for $r = 1.14$. The results of the model for the secondary and higher order instabilities are in qualitative agreement with those obtained from DNS.

We now use the model to investigate the sequence of bifurcations in zero-Prandtl-number convection by varying the rotation rate. We have determined all the fixed points of the model, and carried out their linear stability analysis. The trivial fixed point (i.e., the conduction state) becomes unstable at $r = 1$ and remains unstable for all values of $r > 1$. We have found the possibility of two types of nontrivial fixed points (stationary convective states) in

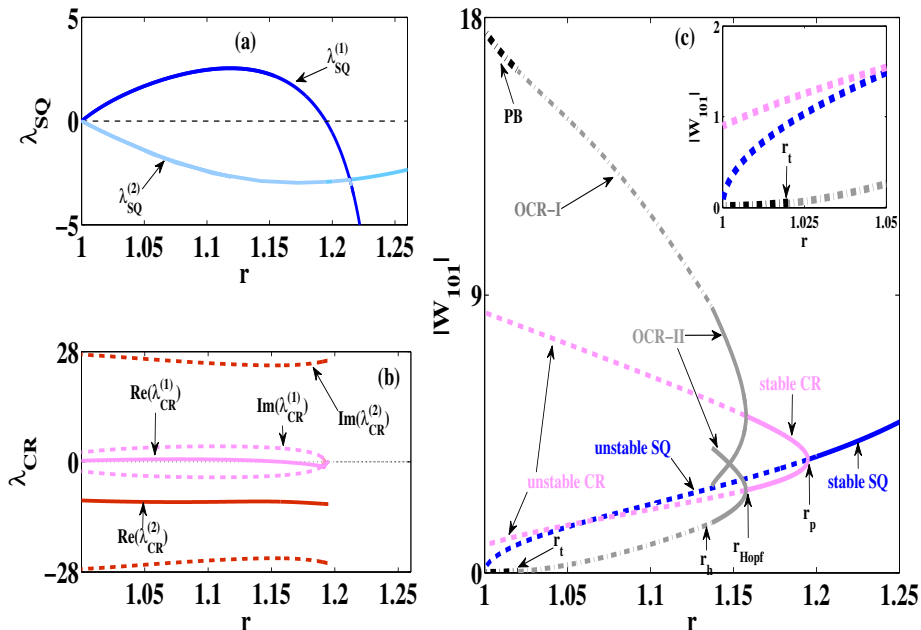


FIG. 12. Linear stability analysis of the nonlinear fixed points of the model for $Ta = 10$ and $\eta = 1$: (a) the variation of the two largest eigenvalues $\lambda_{SQ}^{(1)}$ (blue curve) and $\lambda_{SQ}^{(2)}$ (light blue curve) for the stationary squares (SQ) as a function of r . Both $\lambda_{SQ}^{(1)}$ and $\lambda_{SQ}^{(2)}$ are real. (b) the variation of the two largest eigenvalues $\lambda_{CR}^{(1)}$ (pink curves) and $\lambda_{CR}^{(2)}$ (brown curves) of cross-rolls with r . Both $\lambda_{CR}^{(1)}$ and $\lambda_{CR}^{(2)}$ are complex. Their real parts are shown by solid curves and imaginary parts by broken curves. (c) Bifurcation diagram as obtained from the model. It predicts the PB, OCR-I, OCR-II, CR and SQ patterns as r is raised in small steps.

this model: the square fixed points ($|W_{101}| = |W_{011}|$) and the cross-roll fixed points ($|W_{101}| \neq |W_{011}|$). We now discuss the sequence of bifurcations obtained from the model for $Ta = 10$. The variation of the two largest eigenvalues $\lambda_{SQ}^{(1)}$ and $\lambda_{SQ}^{(2)}$ of the square fixed point with r is shown in figure 12(a) for $Ta = 10$. Both the eigenvalues are found to be real. They vanish at the instability onset ($r = 1$). The largest eigenvalue $\lambda_{SQ}^{(1)}$ (dark blue curve) is positive for $1 < r < 1.195$ and negative for $r \geq 1.195$. The second largest eigenvalue $\lambda_{SQ}^{(2)}$ (light blue curve) is always negative. The square fixed points are therefore stable for $r \geq 1.195$, and become saddle fixed points for $1 < r < 1.195$. The stationary square patterns are observed for $r \geq 1.195$ in the model for $Ta = 10$.

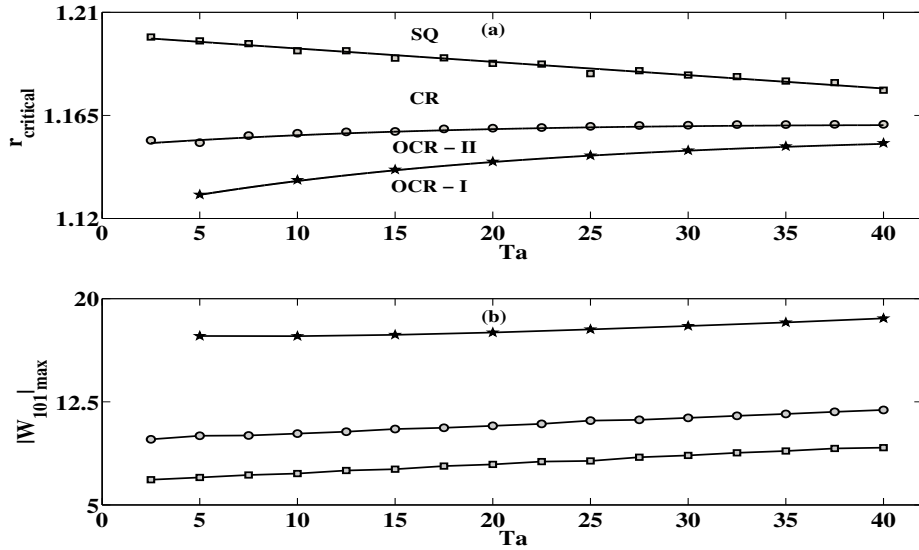


FIG. 13. (a) Variation of the critical value $r_{critical}$ of the reduced Rayleigh number with the Taylor number Ta for different bifurcations ($\eta = 1, L = 2\pi/k_c$). The critical value of r for backward homoclinic bifurcation (line marked by ‘★’) and that for the backward Hopf bifurcation (marked by ‘O’) increase slowly, while the critical value of r for backward pitch-fork bifurcation (‘□’) decreases slowly with increasing Taylor number Ta . (b) Variation of the amplitude of the Fourier mode W_{101} at different bifurcation points (marked by ‘★’, ‘O’ and ‘□’) increases linearly with the Taylor number Ta .

The cross-roll fixed points exist for $1 \leq r \leq 1.194$ for $Ta = 10$. The eigenvalues of the cross-roll fixed points are found to be complex numbers. The eigenvalues with the largest and the second largest real parts are denoted by $\lambda_{CR}^{(1)}$ and $\lambda_{CR}^{(2)}$, respectively. The variations of the real and imaginary parts of $\lambda_{CR}^{(1)}$ (pink curves) and $\lambda_{CR}^{(2)}$ (brown curves) with r are shown in figure 12(b). The real part of $\lambda_{CR}^{(1)}$ is found to be positive for $1 \leq r < 1.158$ and negative only for $1.158 \leq r \leq 1.194$. The real part of $\lambda_{CR}^{(2)}$ is always negative. The imaginary parts of the eigenvalues $\lambda_{CR}^{(1)}$ (pink dashed curves) and $\lambda_{CR}^{(2)}$ (brown dashed curves) remain finite for $r < 1.157$. The stationary cross-roll patterns are observed in the model in the range $(1.158 \leq r \leq 1.194)$ for $Ta = 10$. There are always two sets of cross-rolls: one with $|W_{101}|_{max} > |W_{011}|_{max}$ and another with $|W_{101}|_{max} < |W_{011}|_{max}$. They are connected by a four-fold rotational symmetry in the horizontal plane. The transition from stationary square patterns to stationary cross-rolls occurs at $r = 1.195$ through a pitchfork bifurcation. The

stationary cross-rolls patterns are stable in the range $1.158 \leq r \leq 1.194$. They become unstable at $r = 1.157$ through the Hopf-bifurcation. The unstable cross-roll fixed points are saddle-focus for $1 \leq r \leq 1.157$.

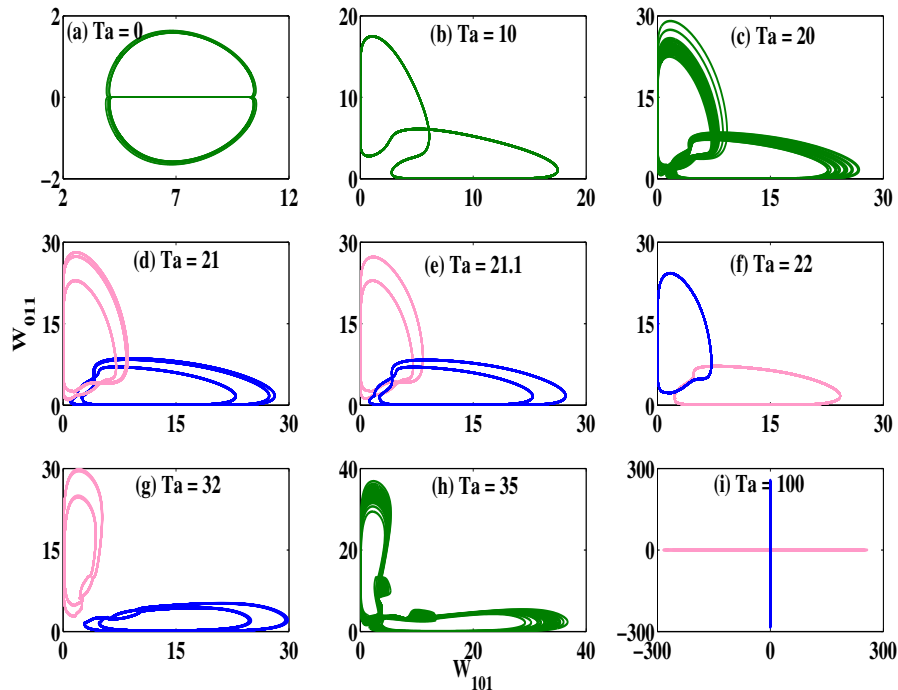


FIG. 14. The projection of the phase portraits on the $W_{101} - W_{011}$ plane near the primary instability ($r = 1.001$) for different values of Ta ($\eta = 1, L = 2\pi/k_c$). Two sets of possible phase plots (blue and pink curves) are possible in each quadrant of the $W_{101} - W_{011}$ plane. The green curves show the glued solutions. The temporal variation of these modes are given in figure 4.

The details of the sequence of bifurcations for $Ta = 10$ are given in the bifurcation diagram [figure 12(c)]. The stable and unstable stationary square patterns are denoted by blue solid and blue dashed curves, respectively. The stable and unstable stationary cross-roll patterns are shown by pink solid and pink dashed curves, respectively. No stationary solution is found to be stable for $r < 1.157$ at $Ta = 10$. We have integrated the model with several different initial conditions to find out the time dependent solutions. Two sets of limit cycles are found to appear at $r = 1.157$ through Hopf bifurcation. The solid dark gray curves in the bifurcation diagram show the maxima and the minima of both the limit cycles, which describe the two branches of oscillating cross-rolls (OCR-II) patterns. We

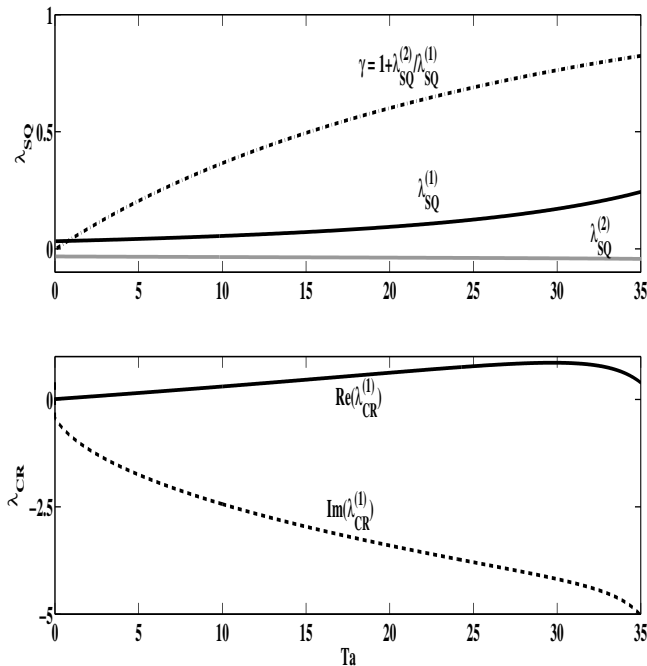


FIG. 15. Linear stability analysis of the nonlinear fixed points of the model near the onset ($r = 1.001$) as a function of Ta for $\eta = 1, L = 2\pi/k_c$. The upper row shows the variation of the two largest eigenvalues $\lambda_{SQ}^{(1)}$ (black curve) and $\lambda_{SQ}^{(2)}$ (gray curve) for the stationary squares (SQ) as a function of Ta . Both $\lambda_{SQ}^{(1)}$ and $\lambda_{SQ}^{(2)}$ are real. The saddle index $\gamma = 1 + \lambda_{SQ}^{(2)}/\lambda_{SQ}^{(1)}$ (broken curve) remains always positive. Eigenvalues with the largest real parts form a complex-conjugate pair in case of cross-rolls (CR) fixed points. The variations of their real and imaginary parts with Ta are shown in the lower row. The real $Re(\lambda_{CR})$ and the imaginary parts $Im(\lambda_{CR})$ are displayed by solid and dashed black curves, respectively.

observe a pattern with either $|W_{101}|_{max} > |W_{011}|_{max}$ or $|W_{101}|_{max} < |W_{011}|_{max}$. The size of both the limit cycles grows, as r is lowered. Both the limit cycles almost touch the square (saddle) fixed points at $r = 1.137$. They simultaneously become homoclinic orbits of the same saddle fixed point. Two limit cycles are spontaneously glued together to form a larger limit cycle. The homoclinic gluing also occurs in the absence of rotation¹⁵. The homoclinic gluing has also been observed in other systems⁵²⁻⁵⁴. The resulting oscillating cross-rolls (OCR-I) have $|W_{101}|_{max} = |W_{011}|_{max}$ and $|W_{101}|_{min} = |W_{011}|_{min} \neq 0$. These patterns (OCR-I) exist for $1.05 < r < 1.137$. Figure 11(e) and 11(f) show the single glued limit cycle and

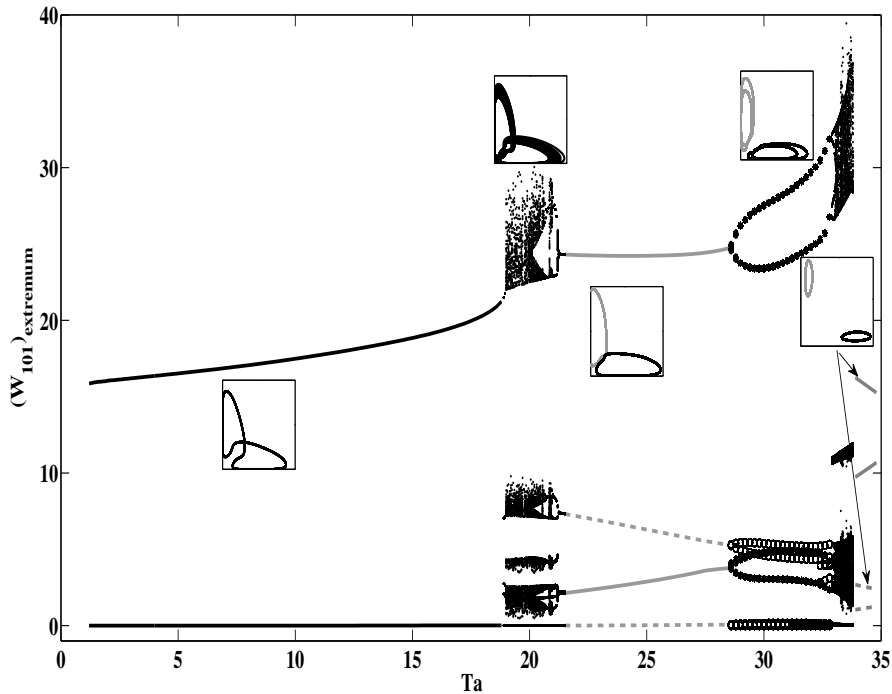


FIG. 16. The bifurcation diagram as a function of Ta , as obtained from the model-I for $r = 1.001$ and $\eta = 1$. The variations extrema of the Fourier mode W_{101} with Ta show glued limit cycle (black solid curves), unglued limit cycles (gray solid and broken curves), period doubling of unglued limit cycles (shown by $*$ and \circ) and chaotic solutions (black \bullet). Typical phase portraits in the $W_{101} - W_{011}$ plane are also shown in square boxes for different windows in Ta .

two unglued limit cycles, respectively. The glued limit cycle exists for $1 < r < 1.137$. The global maximum and minimum of the glued limit cycle are shown by dashed-dotted light gray curves in the bifurcation diagram. The minimum of the glued limit cycle vanishes as r is lowered below 1.02. In this case, the glued limit cycle describes a periodic relaxation oscillation. The amplitude of one set of rolls remains zero for finite time, while that of the other set keeps growing. A set of new rolls gets excited, if the amplitude of the old set of rolls exceeds a critical value. This behavior continues up to the instability onset. It would be interesting to derive a normal form of amplitude equations that captures the phenomenon of critical bursting.

There is a smooth transition from oscillating cross-rolls (OCR-I) to PB of rolls in mutually perpendicular directions at $r = 1.02$. The periodic bursting of patterns is a nonlocal solution

of the hydrodynamic system at the instability onset. The normal form of the amplitude equations in the $Pr \rightarrow 0$ limit with stress-free boundaries is, therefore, non-trivial. It cannot be derived using a local bifurcation analysis of the stationary conduction state. The sequence of bifurcations for a fixed value of Ta consists of a nonlocal bifurcation at the onset, an inverse homoclinic bifurcation from a glued solution to two possible nonlocal solutions, an inverse Hopf bifurcation, and an inverse pitch-fork bifurcation, as r is raised in small steps. The convective patterns consist of the PB, OCR-I, OCR-II, CR and SQ patterns. The transition from the PB patterns to OCR-I patterns is smooth. Figure 13(a) shows the variation of the different bifurcation thresholds with Ta . The threshold for homoclinic bifurcation and the appearance of stationary cross-rolls increases with Ta , while that for the stationary square patterns decreases with increasing Ta . The maximum magnitude of the Fourier mode W_{101} increases with Ta at the onset of different bifurcations [see fig. 13(b)].

We have also used the model to investigate the bifurcations near onset as a function of Ta . The phase portraits obtained by the model for $r = 1.001$ at different values of Ta are shown in figure 14. The model captures the qualitative behaviour observed in DNS (see figure 5). The variations of the eigenvalues of the square (SQ) and cross-rolls (CR) fixed points with Ta are shown in figure 15. The largest eigenvalue $\lambda_{SQ}^{(1)}$ is real and positive, while the second largest eigenvalue $\lambda_{SQ}^{(2)}$ is always negative (see the upper row of figure 15). The square patterns are saddle fixed points near the onset ($r = 1.001$). The two largest eigenvalues of the cross-roll fixed points are found to form complex conjugate pairs for different values of Ta near the onset. The variations of the real $[\text{Re}(\lambda_{CR})]$ and imaginary $[\text{Im}(\lambda_{CR})]$ parts with Ta are shown in the lower row of figure 15. The cross-rolls fixed points are unstable near the onset. The saddle index $\gamma = 1 + \lambda_{SQ}^{(2)}/\lambda_{SQ}^{(1)}$ is found to be always positive near the onset. The nonlinear solutions of the model near onset are obtained by integrating the model. The bifurcation diagram obtained from the model with Ta as a bifurcation parameter is shown in figure 16. The solution near the primary instability can be periodic glued solution, chaotic solution, period doubling of unglued solutions, etc. The nature of the solution depends upon the value of Ta . The model captures the sequence of bifurcations observed in DNS quite well for smaller values of Ta .

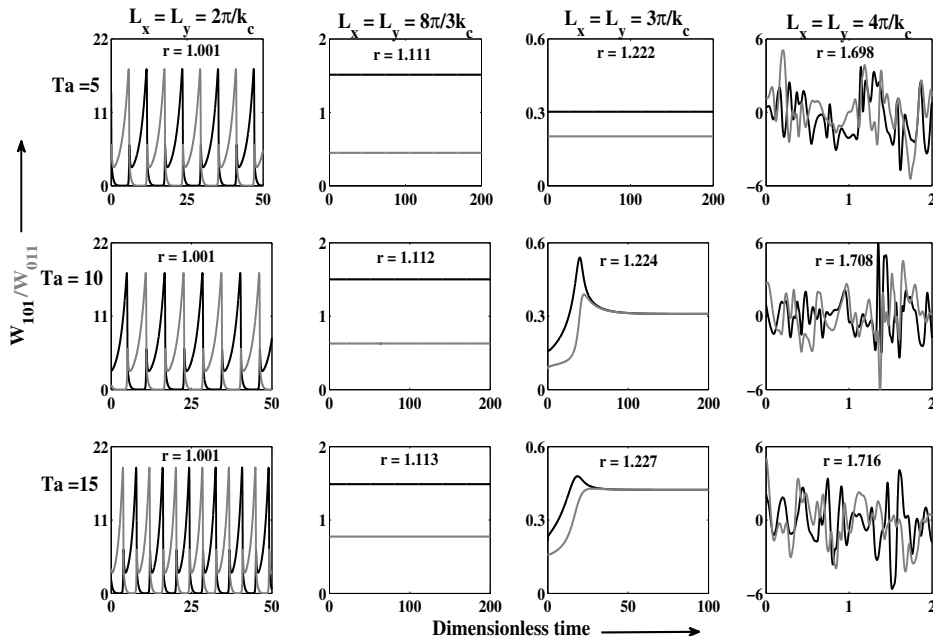


FIG. 17. The temporal variations of Fourier modes W_{101} (black curve) and W_{011} (gray curve) near the onset of convection [$Ra = 1.001 \times Ra_s(Ta, k)$] for different values of Ta in a square simulation box of side length L , as obtained from the model. $Ra_s(Ta, k)$ is threshold value of Ra for a given value of $k < k_c$ and Ta . The temporal variations of the Fourier modes for $L = \lambda_c, 4\lambda_c/3, 3\lambda_c/2$ and $2\lambda_c$ are shown in the first, second, third and the fourth columns, respectively. Curves for $Ta = 5, 10$, and 15 are shown in the first, second, and the third rows, respectively.

B. The model with $L > \lambda_c$

The direct numerical simulations have shown that different nonlinear modes were excited in a rectangular simulation box as the ratio η was varied. The model would require different additional modes at different rotation rates for larger simulation boxes to capture accurately even the primary instability. We have used the model to investigate the effects in larger simulation boxes with $\eta = 1$. We have varied each side L of a square cross-section of the box from $\lambda_c = 2\pi/k_c$ to $2\lambda_c$ for a given value of Ta . The larger simulation boxes describe the convection away from the critical point, when the convection may grow with wave numbers $k < k_c$. The results obtained from the model near onset of convection [$Ra/Ra_s(Ta, k) = 1.001$] for different values of Ta are shown in figure 17, where $Ra_s(Ta, k)$ is threshold value of Ra for stationary convection at a given value of $k < k_c(Ta)$ and Ta .

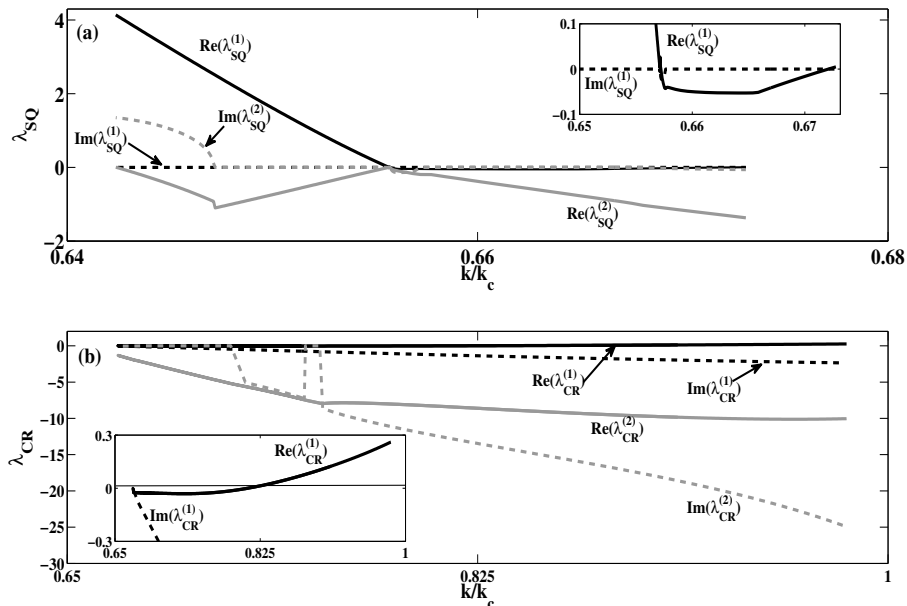


FIG. 18. Linear stability analysis of the nonlinear fixed points of the model near the onset ($Ra/Ra_s(k) = 1.001$) as a function of k for for $Ta = 10$. The upper row shows the variation of the two largest eigenvalues $\lambda_{SQ}^{(1)}$ (black curve) and $\lambda_{SQ}^{(2)}$ (gray curve) for the stationary squares (SQ) as a function of k/k_c . The largest eigenvalue $\lambda_{SQ}^{(1)}$ is real for the whole range of k/k_c . It is negative in a small range k/k_c ($0.657 \leq k/k_c \leq 0.670$). The second largest eigenvalues $\lambda_{SQ}^{(2)}$ is complex for lower values of k/k_c . However, its real part is always negative. The lower row shows the variation of the two largest eigenvalues $\lambda_{CR}^{(1)}$ (black curve) and $\lambda_{CR}^{(2)}$ (gray curve) for the stationary cross-rolls as a function of k/k_c . Both eigenvalues are complex but the largest eigenvalue has negative real part for $0.671 \leq k/k_c \leq 0.810$.

Note that the convection in such cases appear at relatively higher values of r , although $Ra/Ra_s(Ta, k) = 1.001$ for the all cases shown in figure 17. We observe critical bursting of fluid patterns for $L = 2\pi/k_c = \lambda_c$, stationary cross-rolls for $L = 4\lambda_c/3$, stationary square patterns for $L = 3\lambda_c/2$, and chaotic patterns for $L = 2\lambda_c$ at the primary convection. Stationary square patterns were observed in experiments in a container with circular cross-section by Bajaj et al.⁴⁴. The leading Fourier modes of the chaotic patterns for $L = 2\lambda_c$ fluctuates about zero mean, but patterns always appear as squares. It is interesting to note that Sánchez-Álvarez et al.³⁰ also observed chaotically varying square patterns in DNS with realistic boundary conditions in a cylindrical container. The results of the model are in

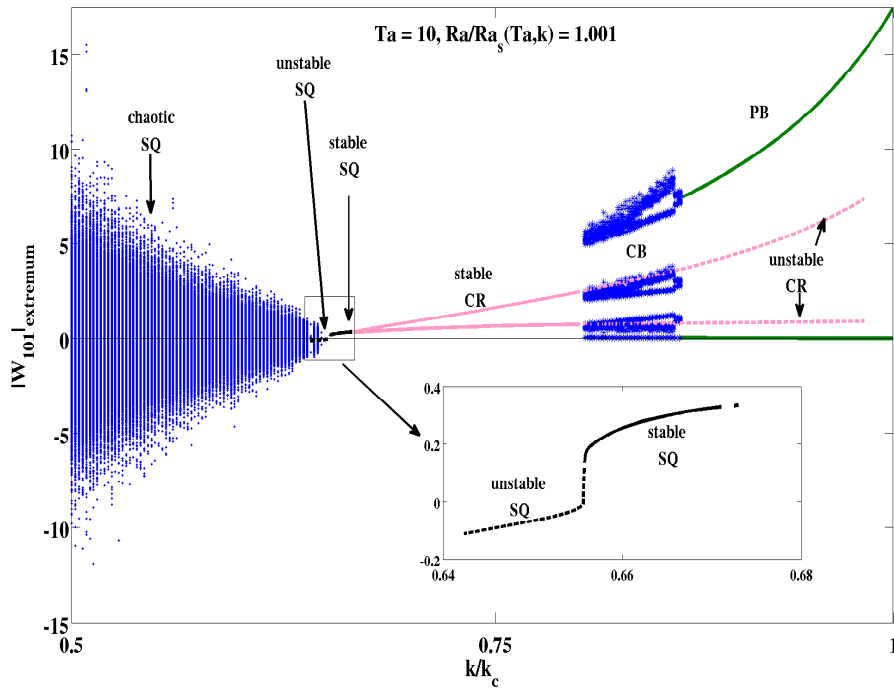


FIG. 19. The bifurcation diagram as a function of $k/k_c(Ta)$, as obtained from the model for $Ra/Ra_s(Ta, k) = 1.001$ and $Ta = 10$. The variation of extrema of the Fourier mode W_{101} with k/k_c show PB (green curves), CB (blue stars), CR (pink curves), SQ (black curves) and chaotic SQ (shown by blue dots). The stable and unstable square fixed points are shown by solid and dashed curves, respectively (please see the inset).

qualitative agreement with those observed in DNS. This signifies the appropriate selection of modes. The model would also be useful in investigating the effects of variation of the horizontal cross-section of a three dimensional simulation box on pattern selection near onset. This type of model would be useful to investigate pattern dynamics near homoclinic bifurcation (e.g. in Taylor-Couette flow). It would be also applicable to investigate the interaction of stationary and oscillatory instabilities in several systems (e.g., convection in binary fluid mixtures, hydromagnetic convection, etc) near a codimension-2 point.

We did the linear stability analysis of the square and cross-roll patterns. We computed using the model the eigenvalues of stability matrix for SQ and CR patterns as a function of $k/k_c(Ta)$ at a given value of $Ra = 1.001Ra_s(k, Ta)$ and Ta . This investigation would reveal the effects of varying the horizontal cross-section on pattern selection. The upper row of

figure 18 shows the variation of the two largest eigenvalues of square fixed points with k/k_c for $Ta = 10$, and the lower displays the variation of the two largest eigenvalues of cross-rolls patterns with k/k_c . This reveals that stationary square patterns are stable in small windows of k/k_c ($0.657 \leq k/k_c \leq 0.670$) and cross-rolls are stable for $0.671 \leq k/k_c \leq 0.810$. The prediction of linear stability analysis explains the stationary values of the largest Fourier modes in figure 17.

Figure 19 shows the bifurcation diagram with k/k_c as bifurcation parameter for $Ra/Ra_s(k) = 1.001$ at a fixed value of $Ta = 10$. As k/k_c decreases for a fixed value of Ta and $Ra/Ra_s(k)$, we observe a sequence of bifurcations. This leads to possibility of variety of patterns: PB, CB, CR, SQ and chaotic square patterns. The model suggests that stationary square patterns are stable in a very narrow window of k/k_c . We could not search stationary square patterns in DNS. It is not easy to search that in parameter space of Ta, Ra, k . However, the model showed the possibility of selection different patterns as L is varied. This may be a possible reason for observing bursting⁴⁵ and stationary square patterns⁴⁴ in rotating RBC.

VII. MODEL-II: A MINIMUM-MODE MODEL NEAR ONSET FOR $Ta < 10$

We now try to make a minimum-mode model which captures the convective dynamics near onset of convection for smaller values of $Ta (< 10)$. The purpose is to understand the behaviour near onset as $Ta \rightarrow 0$. We expand the vertical velocity (v_3) and the vertical vorticity (ω_3) fields as follows:

$$v_3 = W_{101} \cos(kx) \sin(\pi z) + W_{011} \cos(ky) \sin(\pi z) + W_{112} \cos(kx) \cos(ky) \sin(2\pi z) \\ + W_{211} \cos(2kx) \cos(ky) \sin(\pi z) + W_{121} \cos(kx) \cos(2ky) \sin(\pi z), \quad (20)$$

$$\omega_3 = Z_{110} \sin(kx) \sin(ky) + Z_{112} \sin(kx) \sin(ky) \cos(2\pi z) \\ + Z_{211} \sin(2kx) \sin(ky) \cos(\pi z) + Z_{121} \sin(kx) \sin(2ky) \cos(\pi z). \quad (21)$$

where we have put $k = k_c(Ta)$, as done earlier. Projecting the hydrodynamic system (Eqs 16-17) on these modes, we get a dynamical system consisting of nine modes. We then adiabatically eliminate the mode W_{112} , which has the highest linear decay rate. In addition, we found its amplitude of oscillation much smaller than that of other modes. This leads to the following eight-mode model:

$$\begin{aligned} \begin{bmatrix} \dot{X}_1 \\ \dot{X}_2 \end{bmatrix} &= \epsilon(r) \begin{bmatrix} X_1 \\ X_2 \end{bmatrix} - a_1(U - 2V) \begin{bmatrix} X_2 \\ -X_1 \end{bmatrix} + (a_2V + a_3U) \begin{bmatrix} Y_1 \\ -Y_2 \end{bmatrix} - \frac{\pi}{40a_0}(U + 2V) \begin{bmatrix} Z_1 \\ Z_2 \end{bmatrix} \\ &\quad - \frac{c_0}{\delta(r)} \left(10\pi \begin{bmatrix} X_2 \\ X_1 \end{bmatrix} - a_4 \begin{bmatrix} Y_1 \\ Y_2 \end{bmatrix} + a_5 \begin{bmatrix} Z_1 \\ -Z_2 \end{bmatrix} \right) f(\mathbf{X}, \mathbf{Y}, \mathbf{Z}), \end{aligned} \quad (22)$$

$$\begin{aligned} \begin{bmatrix} \dot{Y}_1 \\ \dot{Y}_2 \end{bmatrix} &= -\gamma(r) \begin{bmatrix} Y_1 \\ Y_2 \end{bmatrix} - (b_1U + b_2V) \begin{bmatrix} X_1 \\ -X_2 \end{bmatrix} - (b_3U + b_4V) \begin{bmatrix} Y_2 \\ -Y_1 \end{bmatrix} + \frac{9\pi}{40b_0}(U + 2V) \begin{bmatrix} Z_2 \\ Z_1 \end{bmatrix} \\ &\quad - \frac{c_0}{\delta(r)} \left(b_5 \begin{bmatrix} X_1 \\ X_2 \end{bmatrix} + 9\pi \begin{bmatrix} Y_2 \\ Y_1 \end{bmatrix} - 3 \begin{bmatrix} Z_2 \\ -Z_1 \end{bmatrix} \right) f(\mathbf{X}, \mathbf{Y}, \mathbf{Z}), \end{aligned} \quad (23)$$

$$\begin{aligned} \begin{bmatrix} \dot{Z}_1 \\ \dot{Z}_2 \end{bmatrix} &= -b_0 \begin{bmatrix} Z_1 \\ Z_2 \end{bmatrix} + \frac{\pi}{4}(5U + 4V) \begin{bmatrix} X_1 \\ X_2 \end{bmatrix} - \frac{\pi}{40}(9U + 8V) \begin{bmatrix} Y_2 \\ Y_1 \end{bmatrix} - \frac{9}{80}(U + 2V) \begin{bmatrix} Z_2 \\ -Z_1 \end{bmatrix} \\ &\quad - \frac{\pi c_0}{\delta(r)} \left(9 \begin{bmatrix} Z_2 \\ Z_1 \end{bmatrix} + 10\pi \begin{bmatrix} X_1 \\ -X_2 \end{bmatrix} - 27\pi \begin{bmatrix} Y_2 \\ -Y_1 \end{bmatrix} \right) f(\mathbf{X}, \mathbf{Y}, \mathbf{Z}), \end{aligned} \quad (24)$$

$$\dot{U} = -2c_0U - \frac{\pi^2}{5}(X_1Y_1 - X_2Y_2) - \frac{2\pi}{5}(X_1Z_1 + X_2Z_2), \quad (25)$$

$$\dot{V} = -2k_c^2V + \frac{\pi^2}{5}(X_1Y_1 - X_2Y_2) - \frac{\pi}{10}(X_1Z_1 + X_2Z_2) - \frac{\pi}{20}(Y_1Z_2 + Y_2Z_1), \quad (26)$$

$$\begin{aligned} f(\mathbf{X}, \mathbf{Y}, \mathbf{Z}) &= 200\pi a_0 X_1 X_2 + 18\pi b_0 Y_1 Y_2 + 18\pi Z_1 Z_2 + a_6(X_1 Z_1 - X_2 Z_2) \\ &\quad + a_7(Y_1 Z_2 - Y_2 Z_1) + a_8(X_1 Y_1 + X_2 Y_2), \end{aligned} \quad (27)$$

where $\mathbf{X} = [X_1, X_2]^T \equiv [W_{101}, W_{011}]^T$, $\mathbf{Y} = [Y_1, Y_2]^T \equiv [W_{211}, W_{121}]^T$, $\mathbf{Z} = [Z_1, Z_2]^T \equiv [Z_{211}, Z_{121}]^T$, $U \equiv Z_{112}$, and $V \equiv Z_{110}$. The coefficients which depend on the reduced Rayleigh number are: $\epsilon(r) = [(3r - 1)k_c^2 - \pi^2]$, $\gamma(r) = [b_0^3 - 15a_0^2 k_c^2 r]/b_0^2$, and $\delta(r) = 4000(4c_0^3 - 3a_0^2 k_c^2 r)$. Other coefficients which depend on $k_c(Ta)$ are defined as: $a_0 = \pi^2 + k_c^2$, $b_0 = \pi^2 + 5k_c^2$, $c_0 = 2\pi^2 + k_c^2$, $a_1 = (\pi^2 - k_c^2)/(8a_0)$, $a_2 = (5k_c^2 - \pi^2)/(40a_0)$, $a_3 = (9\pi^2 - 5k_c^2)/(80a_0)$, $a_4 = \pi(11\pi^2 - 17k_c^2)/a_0$, $a_5 = (3\pi^2 - k_c^2)/a_0$, $a_6 = 10(4\pi^2 - k_c^2)$, $a_7 = 3(8\pi^2 - 5k_c^2)$, $a_8 = 20\pi(\pi^2 + 11k_c^2)$, $b_1 = 5(\pi^2 - k_c^2)/(8b_0)$, $b_2 = (3\pi^2 + 5k_c^2)/(4b_0)$, $b_3 = 3(13\pi^2 - 25k_c^2)/(80b_0)$, $b_4 = 3(3\pi^2 + 25k_c^2)/(40b_0)$, and $b_5 = 10\pi(13\pi^2 + 5k_c^2)/b_0$.

The elimination of any other mode leads to significantly different solutions from those observed in DNS. We therefore call this minimum-mode model as model-II. Table III shows

a comparison between the results obtained from DNS and the two models (model-I and model-II) for $r = 1.001$. Though the model-II (Eqs. 22-26) shows larger deviations from the results obtained from DNS, it qualitatively captures the features observed in DNS just above onset ($r \leq 1.001$) for very small values of Taylor numbers ($0 \leq Ta \leq 10$). The temporal variations of the two largest Fourier modes W_{101} and W_{011} for four different values of Ta obtained from model-II and the corresponding phase projections are plotted in figure 20.

TABLE III. Comparison of models and DNS. The global extrema of the Fourier mode W_{101} and the period τ of bursting obtained from DNS, model-I and model-II are compared for different values of the Taylor number Ta .

Ta	Max(W_{101})			Min(W_{101})			Period of bursting (τ)		
	DNS	Model-I	Model-II	DNS	Model-I	Model-II	DNS	Model-I	Model-II
0	11.05	10.56	10.34	2.83	3.89	4.20	-	-	-
3	15.36	16.20	14.45	0	0	0	38.66	35.76	27.60
5	15.97	16.52	14.56	0	0	0	24.35	22.41	17.42
6	16.27	16.69	14.69	0	0	0.001	20.67	18.91	14.80
8	16.78	17.06	14.88	0	0	0.005	15.84	14.45	11.40
10	17.38	17.48	15.11	0.001	0.002	0.018	12.87	11.77	9.30

The onset for $Ta \rightarrow 0$ limit is always found to be chaotic, while periodic solutions exist for $2 < Ta \leq 10$. These results are in agreement with the behaviour observed in DNS for $Ta \leq 10$ (please see figures 4 and 5). The minimum-mode model, which does not capture the dynamics of the system accurately at higher values of r and Ta , may be used to study the dynamics just near onset for smaller values of Ta .

A. Bursting of fluid patterns near onset

The first row of figure 20 shows the variation of the 2D roll modes W_{101} and W_{011} with time, and the second row gives the phase portrait in the $W_{101} - W_{011}$ plane for $r = 1.001$. The mode W_{011} varies almost periodically about a finite mean, while the mode W_{101} varies chaotically with zero mean for $Ta \leq 0.8$. The corresponding phase portrait is shown in the

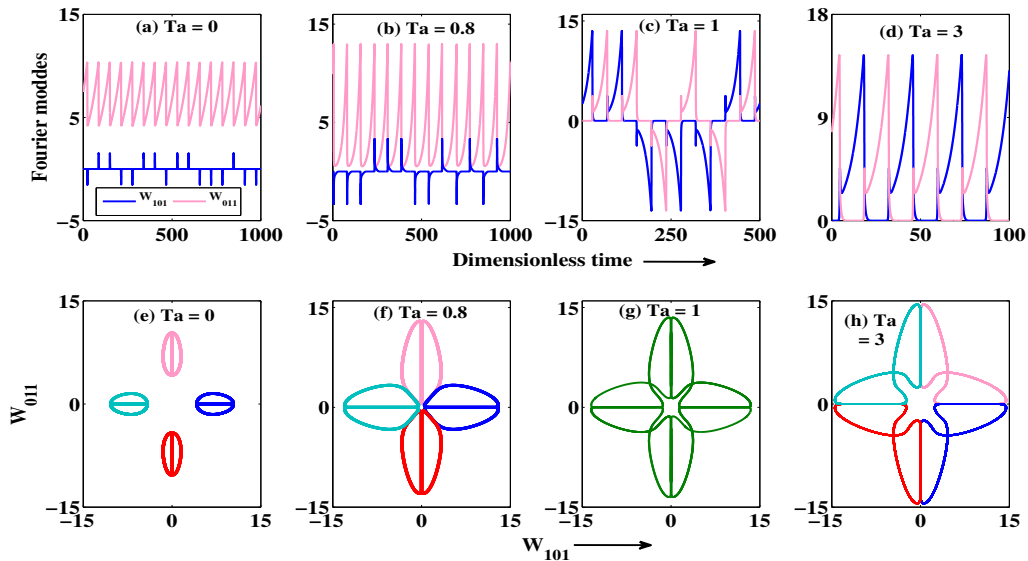


FIG. 20. Results obtained from the model-II near the onset $r = 1.001$ for four different values of Ta . First row of the figure shows the temporal variation of two largest Fourier modes W_{101} and W_{011} for (a) $Ta = 0$, (b) $Ta = 0.8$, (c) $Ta = 1$ and (d) $Ta = 3$. The corresponding phase projections on $W_{101} - W_{011}$ plane are plotted in the second row of the figure.

pink color in fig. 20 (e). Changing W_{011} to $-W_{011}$ leads to red colored loops. Interchanging W_{011} and W_{101} also lead to similar dynamics. The dark blue and light blue colored loops represent them. Depending on initial conditions any one of four possible sets of chaotic solutions is possible. Each set represents a chaotic solution here. The chaos occurs due to the random sequence of one of the most dangerous mode (W_{101} or W_{011}). This is also an example of heteroclinic chaos with an additional feature: one of the 2D roll mode vanishes for finite time. As Ta is raised in small steps, these orbits grow in size. This behaviour persists for $0 < Ta < 0.9$. Figure 20 (b) and (f) show the temporal variation of 2D roll modes and the phase portrait respectively for $Ta = 0.8$.

For $Ta = 0.9$, all the four chaotic solutions spontaneously merge together. Either maximum or minimum of both the 2D roll modes is zero for finite time. Figure 20 (c) and (g) show such a chaotic solution and corresponding phase portrait respectively for $Ta = 1.0$. This represents a chaotic bursting⁴⁵ of patterns at the primary instability. One set of rolls suddenly vanishes and another set of rolls perpendicular to the old sets appears. The old set of rolls is again excited after a finite time, as the amplitude of the new set of rolls reaches a

critical value. This is different than standard Küppers-Lortz instability, where fluid patterns do not show the phenomenon of bursting of patterns as described by Bajaj et al.⁴⁵. This is an example of merging of heteroclinic chaos in Rayleigh-Bénard convection with rotation. The trajectory now wanders around all four saddle fixed points. As Ta is further raised, the merged chaotic solution spontaneously breaks into one of the possible four limit cycles for $Ta = 2.1$. Figure 20 (d) and (h) displays the temporal variation of the two largest modes and the possibility of four possible limit cycles in different colors for $Ta = 3$. Each of the 2D modes vanishes at regular interval and does grow for finite time. This leads to bursting of patterns at regular interval. This behaviour continues till $Ta = 10$.

B. Estimate of the time period of regular bursting of patterns

The mode W_{101} , which appear like a ‘delta function’ in fig. 20 (a) in the absence of rotation, is excited only when the mode W_{011} grows close to its maximum value. It is also evident from the model-II that only the two largest Fourier modes W_{101} and W_{011} have positive growth rate ϵ as soon as $r > 1$. All the other modes decay linearly. Just after the mode W_{101} is excited, the mode W_{011} falls to its minimum value very quickly. The time of growth of rolls from its minimum intensity to the maximum is quite different from the time of decay from its maximum to minimum intensity. In the presence of even small rotation ($0 < Ta < 1$), the minimum intensity of atleast one set of rolls becomes zero [see figs. 20 (b)-(d)] and remains zero for finite time. This is an example of bursting of patterns near onset. The phenomenon of bursting involves two time scales: growth time τ_1 and bursting time τ_2 . As long as $\tau_2 \ll 0.15\tau_1$, the bursting of fluid patterns is irregular. When $\tau_2 \sim 0.15\tau_1$, the bursting of patterns occurs at a regular interval. The time period of the regular bursting is then estimated as: $\tau = 2 \times (\tau_1 + \tau_2) \approx 2.3\tau_1$. The factor 2 appears because a pattern repeats after bursting of two sets of rolls in mutually perpendicular directions [see fig. 20 (d)]. We estimate the period by taking τ_1 equal to the inverse of the linear growth rate. We begin with the largest linear growth rate σ_+ (eq. 7). Writing $Ra = r \times Ra_c$ and setting $k = k_c$, the expression for σ_+ reads as:

$$\sigma_+ = \frac{-2(\pi^2 + k_c^2)^3 + k_c^2 r Ra_c + \sqrt{(k_c^2 r Ra_c)^2 - 4\pi^2(\pi^2 + k_c^2)^3 Ta}}{2(\pi^2 + k_c^2)^2}. \quad (28)$$

For smaller values of Taylor numbers ($Ta < 10$), $(k_c^2 r Ra_c)^2 \gg 4\pi^2(\pi^2 + k_c^2)^3 Ta$ near the onset ($r \approx 1$). Ignoring $4\pi^2(\pi^2 + k_c^2)^3 Ta$ with respect to $(k_c^2 r Ra_c)^2$ in the expression for σ_+ and using Eq. 10 leads to $\sigma_+ \rightarrow \epsilon(r) = (3r - 1)k_c^2(Ta) - \pi^2$. Binomially expanding the expression for $k_c(Ta)$ (Eq. 11) in Ta and retaining terms upto cubic order yield

$$\epsilon(r, Ta) = \frac{3\pi^2(r-1)}{2} + \frac{2(3r-1)}{9\pi^2}Ta - \frac{8(3r-1)}{9\pi^6}Ta^2 - \frac{(3r-1)}{9\pi^{10}}Ta^3 + \mathcal{O}(Ta^4). \quad (29)$$

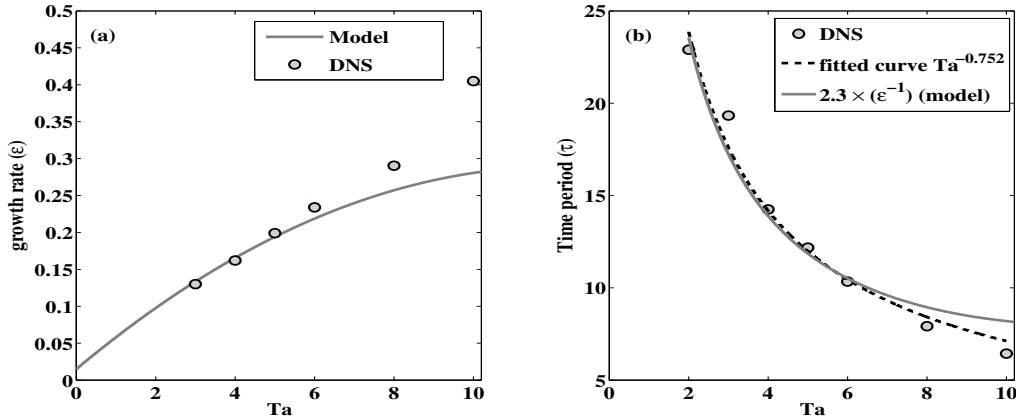


FIG. 21. Comparison of growth rates and time periods (τ) of the two largest modes W_{101} or W_{011} at the onset ($r = 1.001$) as obtained from the model II using eq. 29 and DNS.

The time constant for the exponential growth of the rolls is $\tau_1 = 1/\epsilon(r)$, and the period of regular bursting is $\tau \approx 2.3/\epsilon(r)$. The linear growth rate of the largest mode just above the onset is therefore given as: $\epsilon(r \rightarrow 1, Ta) = 4Ta/(9\pi^2) - 16Ta^2/(9\pi^6) - 2Ta^3/(9\pi^{10})$. Figure 21 (a) shows a comparison of the linear growth rate $\epsilon(r)$ of the model-II (gray solid curve) and the exponential growth rate extracted from DNS (circles). The deviation of growth rates obtained from the model-II and DNS become clearly visible for $Ta > 7$. Figure 21 (b) shows the comparison of the time periods of bursting of patterns for $r = 1.001$ obtained from model-II (gray solid curve) and DNS (circles). A curve (dashed line) fitted to the DNS data shows $\tau \sim Ta^{-0.752}$ for smaller values of Ta . Actually the period τ involves polynomial in Ta . The model also shows that the period of oscillation would be finite for any Ta , if $r - 1$ is not negligible. The limit $Ta \rightarrow 0$ is not meaningful as periodic bursting is not observed for $Ta \leq 2$. Figure 7 showed that the period τ of bursting near onset for larger range of Ta ($2 < Ta \leq 40$), after omitting the data points for chaotic bursts, scaled with Ta as $Ta^{-0.784}$. The vertical vorticity modes linearly coupled to the vertical velocity also become

significant for relatively higher values of Ta , and the linear growth rate is modified. This in turn changes the time constant τ_1 . The frequency of oscillatory convection (Eq. 12) is imaginary for $Ta < 328$. The bursting of patterns is therefore not the consequence of the oscillatory convection at onset. It is due the instability of a set of growing rolls due to the generation of vertical vorticity, as the amplitude of the 2D rolls crosses a critical value.

C. Bifurcation of bursting patterns

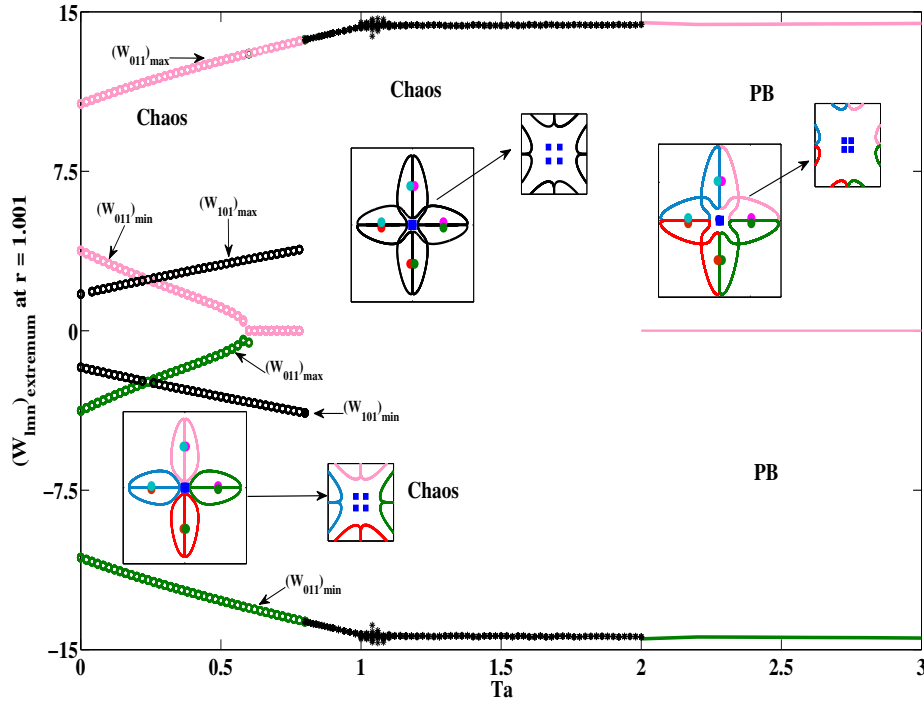


FIG. 22. Bifurcation diagram at the onset ($r = 1.001$) obtained from the minimum-mode model (model-II) with Ta as the bifurcation parameter. Two possible sets of extrema for the mode W_{011} are marked as pink and green ‘o’ for $0 \leq Ta \leq 0.8$. The extrema for mode W_{101} for the same range of Ta are shown in black ‘o’. For $0.8 < Ta \leq 2$, both the modes have only one set of identical extrema marked by black ‘*’. For $2 \leq Ta < 15$, two sets of identical extrema (pink and green curves) are possible for both the modes, and one of them is always zero. The typical phase portraits for different solutions are shown in insets. Blue squares represent saddle squares and dots in different colors represent unstable (saddle focus) cross-rolls.

Figure 22 displays the bifurcation of solutions obtained from model-II near the onset of

convection for $0 \leq Ta \leq 3$, as Ta is varied in small steps. Two sets of possible extrema for the mode W_{011} , marked by pink and green circles, exist for $0 \leq Ta < 0.6$, while only one set of extrema exists for the mode W_{101} in this range of Ta . Typical phase portraits in the $W_{101} - W_{011}$ plane are shown in the first inset by pink and green loops for $0 \leq Ta < 0.6$. Interchange of modes W_{011} and W_{101} give another pair of solutions. The corresponding phase portraits are shown in blue and red loops in the inset. Blue squares in the insets represent four saddle square fixed points, one in each quadrant of the $W_{101} - W_{011}$ plane. Dots in different color represent eight saddle focus (cross-rolls) fixed points, two in each quadrant of the $W_{101} - W_{011}$ plane. Each loop represents a possible chaotic solution, as W_{101} varies chaotically with time. Each loop comes close to each other as Ta is raised slowly. For $0.6 < Ta < 0.8$, the minima of of the upper branch W_{011} (shown by pink circles) and the maxima of the lower branch (shown by green circles) become zero. Each loop touches the a pair of saddle fixed points. We have four distinct sets of possible heteroclinic chaotic solutions for $0.6 < Ta \leq 0.8$. This is when the fluid patterns show the phenomena of bursting. As the value of Ta is raised above 0.8, four distinct sets of chaotic solutions merge together to form another chaotic solution. The typical phase portrait of this situation is shown by black curves in the second inset. The modes W_{011} and W_{101} have identical extrema but they have a phase difference [see Fig. 20 (c)]. As the value of Ta is raised above 2, the merged chaotic solution spontaneous break into one of four possible limit cycles (periodic solution), each shown in a different color. This happens when the loops made by chaotic trajectories just touch the square saddle fixed points. This represents an inverse heteroclinic bifurcation. After this bifurcation, each limit cycle is confined to only one quadrant of the $W_{101} - W_{011}$ plane. There is a transition from irregular bursting of patterns to regular bursting of patterns. Bajaj et al.⁴⁵ had also reported the periodic bursting of fluid patterns in their experiments in low-Prandtl-number fluids with rotation. Each limit cycle is closer to only one of of the four saddle square fixed points. This minimum-mode model is not good enough to capture dynamical behaviour away from the onset. Bifurcation diagram shown in Fig. 6 based on model-I shows that the increase in r at a fixed value of Ta in certain range leads to homoclinic merging (OCR-I solution).

The projection of the phase space in the $W_{101} - W_{101}$ plane (Fig. 22) explains the exponential growth of one of 2D roll modes (W_{101} and W_{101}) to a large value followed by sudden fall to zero value. For $r = 1$ ($\epsilon(r = 1) = 0$), all the points on the W_{101} and W_{101} axes are

fixed points for smaller values of Ta ($Ta \rightarrow 0$). The origin represents the conduction state, while other fixed points represent 2D rolls. As r is raised slightly above unity, all these fixed points become unstable. In addition, four saddle fixed points describing unstable square patterns (blue squares) and eight saddle foci describing unstable cross-rolls patterns (dots in different colors) are generated. The four saddle fixed points surround the origin, while a pair of saddle foci are located very closely on two sides of any axis in positive as well as negative directions. The stable and unstable manifolds of these fixed points now decide the dynamics of any trajectory in the phase space. For example, a pair of saddle foci on the two sides of the positive W_{011} axis guide any trajectory starting near origin on this axis to keep moving on the axis in the positive direction to a large positive value. As soon as it crosses a critical values, the vertical vorticity is excited through nonlinearity. This transfers the energy of energy from 2D roll mode W_{011} to another 2D mode W_{101} in a very short time. The trajectory then moves away from the W_{011} axis, makes a loop around the unstable cross-roll fixed point and returns near the origin on the W_{101} axis. The rolls patterns parallel to the y axis disappears and a new set of rolls parallel to the x axis starts growing. The trajectories form, depending upon the value of Ta , either an open but bounded or a closed heteroclinic orbit. They correspond to irregular (chaotic) or regular (periodic) bursting of patterns. As observed in DNS and model-I, the orbit may become either an open or a closed homoclinic orbit for $Ta \geq 10$ (see Fig. 11) near onset.

VIII. CONCLUSIONS

We have investigated the convective patterns at primary instability using direct numerical simulations in zero-Prandtl-number Rayleigh-Bénard convection with uniform rotation. The direct numerical simulations have been done in the viscous regime with stress-free boundary conditions. The convective patterns at the instability onset are found to be time-dependent in this limit. The phenomenon of bursting of fluid patterns has been observed at the onset for small values of $1 < Ta < 40$ in a simulation box with square horizontal cross-section ($\eta = 1$) with each side $L = \lambda_c$. Bursts of large-amplitude convection appeared and then disappeared in mutually perpendicular directions. The bursting of patterns occurs at irregular intervals for certain windows of Ta ($2 \leq Ta \leq 10$ and $28 \leq Ta \leq 40$), while it occurs at a regular interval in some other windows of Ta ($0 \leq Ta \leq 10$ and $10 < Ta < 28$). Increasing r at a

fixed value of Ta ($5 \leq Ta \leq 40$) leads to a series of interesting fluid patterns: merging of two limit cycles (oscillating cross-rolls, OCR-I), spontaneous breaking of the merged limit cycle into one of the possible smaller limit cycles (OCR-II), stationary cross-rolls, and stationary squares.

The pattern dynamics at the onset is different in rectangular simulation boxes. Periodic wavy rolls are observed at the onset for lower values of Ta , while KL patterns are observed at moderate values of Ta for $1/\sqrt{3} \leq \eta \leq 2$. There is a transition from to GKL patterns near a bicritical point. In larger simulation boxes with rectangular horizontal cross-section ($\eta \geq 4$), KL pattern are observed near onset even at smaller values of Ta . The Küppers-Lortz patterns (KL and GKL) also show irregular bursting occasionally. Temporally quasiperiodic patterns are observed in the oscillatory regime ($Ta > 550$) for $\eta = 1$ and 2. In the oscillatory regime ($Ta > 550$) near a bicritical point ($Ra_c(Ta) = Ra_o$), temporally quasiperiodic or chaotic cross-rolls ($|W_{101}| \neq |W_{011}|$) have been observed for $\eta = 1$ and 2. They do not show the phenomenon of bursting of patterns.

We have also presented two low-dimensional models for a square simulation box ($\eta = 1$). A twenty-mode model (model-I) captures the sequence of secondary and higher-order instabilities qualitatively well for $L = 2\pi/k_c$ at smaller rotation rates ($Ta < 50$). The model clearly reveals the origin of bursting. When the amplitude of a set of rolls exceeds a large critical value, the vertical vorticity modes are nonlinearly excited. The bursting involves a nonlocal bifurcation at the primary instability for smaller values of Ta . This also shows a new possibility of large variation of the roll amplitude at a supercritical bifurcation. Increasing r leads to a series of interesting instabilities including inverse homoclinic, inverse Hopf and inverse pitchfork bifurcations. The model also captures the sequence of bifurcations qualitatively at the primary instability as Ta is varied. The model also shows the possibility interesting bifurcations as the parameter k/k_c is varied keeping Ta , r and η fixed. It shows the possibility of stationary cross-rolls for $L = 8\pi/3k_c$ and stationary square patterns for $L = 3\pi/k_c$. This suggests that selection of convective patterns near the onset in rotating convection may be significantly influenced by the size of the horizontal cross-section of the container. The model shows stationary patterns instead of Küppers-Lortz patterns at the onset by varying the horizontal cross-section slightly with fixed values of all other parameters. This type of model would be useful to understand the unfolding of bifurcations near a bicritical point. A minimum-mode model (model-II), effective just above the onset

and for $Ta < 10$ shows interesting dynamics. The model shows heteroclinic chaotic solutions, merging of heteroclinic chaotic solutions, and spontaneous breaking of the merged chaotic solution into a limit cycle solution at the primary instability for $Ta < 10$.

ACKNOWLEDGMENT

We benefited from fruitful discussions with Pinaki Pal, Hirdesh K. Pharasi, Arnab Basak, and Deepesh Kumar.

REFERENCES

- ¹F. H. Busse, “The oscillatory instability of convection rolls in a low Prandtl number fluid,” *J. Fluid Mech.* **52**, 97-112 (1972).
- ²M. R. E. Proctor, “Inertial convection at low Prandtl number,” *J. Fluid Mech.* **82**, 97-114 (1977).
- ³R. M. Clever and F. H. Busse, “Low-Prandtl-number convection in a layer heated from below,” *J. Fluid Mech.* **102**, 61-74 (1981).
- ⁴W. L. Shew and D. P. Lathrop, “Liquid sodium model of geophysical core convection,” *Phys. Earth and Planet. Interiors* **153**, 136-149 (2005).
- ⁵A. Chiffaudel, S. Fauve, and B. Perrin, “Viscous and Inertial Convection at low Prandtl Number: Experimental study,” *Europhys. Lett.* **4**, 555-560 (1987).
- ⁶S. Fauve, E. W. Bolton, M. E and Brachet, “Nonlinear oscillatory convection: A quantitative phase dynamics approach,” *Physica D* **29**, 202-214 (1987).
- ⁷V. Croquette, “Convective pattern dynamics at low Prandtl number: Part I,” *Contemp. Phys.* **30**, 113-133 (1989).
- ⁸A. Libchaber, C. Laroche, and S. Fauve, “Period doubling cascade in mercury, a quantitative measurement,” *J. Phys. Lett. (Paris)* **43**, 211-216 (1982).
- ⁹J. Liu and G. Ahlers, “Spiral-defect chaos in Rayleigh-Bénard convection with small Prandtl numbers,” *Phys. Rev. Lett.* **77**, 3126-3129 (1996).
- ¹⁰H.-W. Xi, X.-J Li, and J. D. Gunton, “Direct Transition to Spatio-temporal Chaos in Low Prandtl Number Fluids,” *Phys. Rev. Lett.* **78**, 1046-1049 (1997).

- ¹¹D. A. Egolf, I. V. Melnikov, W. Pesch, and R. E. Ecke, “Mechanisms of extensive spatio-temporal chaos in Rayleigh-Bénard convection,” *Nature* **404**, 733-736 (2000).
- ¹²O. Thual, “Zero-Prandtl-number convection,” *J. Fluid Mech.* **240**, 229-258 (1992).
- ¹³P. Pal, P. Wahi, S. Paul, M. K. Verma, K. Kumar, and P. K. Mishra, “Bifurcation and Chaos in zero-Prandtl-number convection,” *Europhys. Lett.* **87**, 54003 (2009).
- ¹⁴P. K. Mishra, P. Wahi and M. K. Verma, “Patterns and Bifurcations in low-Prandtl-number Rayleigh-Bénard convection,” *Europhys. Lett.* **89**, 44003 (2010).
- ¹⁵P. Pal, K. Kumar, P. Maity, and S. K. Dana, “Pattern dynamics near inverse homoclinic bifurcation in fluids,” *Phys. Rev. E.* **87**, 023001 (2013).
- ¹⁶Chandrasekhar, S. *Hydrodynamic and Hydromagnetic stability. Dover publications* New York, 1961.
- ¹⁷E. A. Spiegel, “Thermal turbulence at very small Prandtl number,” *J. Geophys. Rev.* **67**, 3063-3070 (1962).
- ¹⁸K. Kumar, S. Fauve, and O. Thual, “Critical self-tuning: the example of zero-Prandtl-number convection,” *J. Phys. II* **6**, 945-951 (1996).
- ¹⁹K. Kumar, P. Pal, and S. Fauve, “Critical bursting,” *Europhys. Lett.* **74**, 1020-1026 (2006).
- ²⁰G. Veronis, “Large-amplitude Bénard convection in a rotating fluid,” *J. Fluid Mech.* **31**, 113-139 (1968).
- ²¹G. Küppers and D. Lortz, “Transition from laminar convection to thermal turbulence in a rotating fluid layer,” *J. Fluid Mech.* **35**, 609-620 (1969).
- ²²G. Küppers, “The stability of steady finite amplitude convection in a rotating fluid layer,” *Phys. Lett.* **32A**, 7-8 (1970).
- ²³H. T. Rossby, “A study of Bénard convection with and without rotation,” *J. Fluid. Mech.* **36**, 309-335 (1969).
- ²⁴D. N. Riahi, “Weakly Nonlinear Oscillatory Convection in a Rotating Fluid,” *Proc. R. Soc. Lond. A.* **436**, 33-54 (1992).
- ²⁵H. F. Goldstein, E. Knobloch, I. Mercader, and M. Net, “Convection in a rotating cylinder. Part 1.Linear theory for low Prandtl numbers,” *J. Fluid Mech.* **262**, 293-324 (1994).
- ²⁶R. M. Clever and F. H. Busse, “Convection in a low Prandtl number fluid layer rotating about a vertical axis,” *Eur. J. Mech. B - Fluids* **19**, 213-227 (2000).
- ²⁷S. M. Cox and P. C. Mathews, “Instability in rotating convection,” *J. Fluid Mech.* **403**, 153-172 (2000).

- ²⁸J. H. P. Dawes “A Hopf/steady-state mode interaction in rotating convection: bursts and heteroclinic cycles in a square periodic domain,” *Physica D* **149**, 197-209 (2001).
- ²⁹J. H. P. Dawes, “Rapidly rotating thermal convection at low Prandtl number,” *J. Fluid Mech.* **428**, 61-80 (2001).
- ³⁰J. J. Sánchez-Álvarez, E. Serre, E. Crespo del Arco, and F. H. Busse “Square patterns in rotating Rayleigh-Bénard convection,” *Phys. Rev. E* **72**, 036307 (2005).
- ³¹J. M. Lopez and F. Marques, “Centrifugal effects in rotating convection: nonlinear dynamics,” *J. Fluid Mech.* **628**, 269-297 (2009).
- ³²H. K. Pharasi and K. Kumar “Oscillatory instability and fluid patterns in low-Prandtl-number Rayleigh-Bénard convection with uniform rotation,” *Phys. Fluids* **25**, 104105 (2013).
- ³³N. Becker, J.D. Scheel, M. C. Cross, and G. Ahlers, “Effect of the centrifugal force on domain chaos in Rayleigh-Bénard convection,” *Phys. Rev. E* **73**, 066309 (2006).
- ³⁴K. Julien, S. Legg, J. McWilliams, and J. Werne, “Rapidly rotating turbulent Rayleigh-Bénard convection,” *J. Fluid Mech.* **322**, 243-273 (1996).
- ³⁵K. Julien, S. Legg, J. McWilliams, and J. Werne, “Hard turbulence in rotating Rayleigh-Bénard convection,” *Phys. Rev. E* **53**, R5557-R5560 (1996).
- ³⁶Y. Liu and R. Ecke, “Heat transport measurements in turbulent rotating Rayleigh-Bénard convection,” *Phys. Rev. E* **80**, 036314 (2009).
- ³⁷E. M. King, S. Stellmach, J. Noir, U. Hansen, and J. M. Aurnou, “Boundary layer control of rotating convection systems,” *Nature* **457**, 301-304 (2009).
- ³⁸R. J. A. M. Stevens, J.-Q. Zhong, H. J. H. Clercx, G. Ahlers, and D. Lohse, “Transitions between Turbulent States in Rotating Rayleigh-Bénard Convection,” *Phys. Rev. Lett.* **103**, 024503 (2009).
- ³⁹H. K. Pharasi, R. Kannan, K. Kumar, and J. K. Bhattacharjee, “Turbulence in rotating Rayleigh-Bénard convection in low-Prandtl-number fluids,” *Phys. Rev. E* **84**, 047301 (2011).
- ⁴⁰E. M. King and J. M. Aurnou, “Turbulent convection in liquid metal with and without rotation,” *PNAS* **110**, 6688-6693 (2013).
- ⁴¹H. K. Pharasi, K. Kumar, and J. K. Bhattacharjee “Entropy and energy spectra in low-Prandtl-number convection with rotation,” *Phys. Rev. E* **89**, 023009 (2014).
- ⁴²F.H. Busse and K.E. Heikes “Convection in a rotating layer: A simple case of turbulence,”

Science **208**, 173-175 (1980).

- ⁴³J.J. Niemela and R.J. Donnelly “Direct transition to turbulence in rotating Bénard convection,” Phys. Rev. Lett. **57**, 2524-2547 (1986).
- ⁴⁴K. M. S. Bajaj, J. Liu, B. Naberhuis, and G. Ahlers, “Square patterns in Rayleigh-Bénard convection with rotation about a vertical axis,” Phys. Rev. Lett. **81**, 806-809 (1998).
- ⁴⁵K. M. S. Bajaj, G. Ahlers, and W. Pesch “Rayleigh-Bénard convection with rotation at small Prandtl numbers,” Phys. Rev. E **65**, 056309 (2002).
- ⁴⁶M. Sprague, K. Julien, E. Knobloch, and J. Werne, “Numerical simulation of an asymptotically reduced system for rotationally constrained convection,” J. Fluid Mech. **551**, 141-174 (2006).
- ⁴⁷J. D. Scheel, P. L. Mutyaba, and T. Kimmell, “Patterns in rotating Rayleigh-Bénard convection at high rotation rates,” J. Fluid Mech. **659**, 24-42 (2010).
- ⁴⁸R.J. Goldstein and D.J. Graham “Stability of a horizontal fluid layer with zero shear boundaries,” Phys. Fluids. **12**, 1133 (1969).
- ⁴⁹M. K. Verma, “Object-oriented pseudo-spectral code TARANG for turbulence simulation,” arXiv:1103.2517 (2011).
- ⁵⁰T. Clune and E. Knobloch “Pattern selection in rotating convection with experimental boundary conditions,” Phys. Rev. E **47**, 2536-2550 (1993).
- ⁵¹J. M. Carlson and J. S. Langer “Properties of earthquake generated by fault dynamics,” Phys. Rev. Lett. **62**, 2632-2635 (1989).
- ⁵²G. Demeter and L. Kramer, “Transition to Chaos via Gluing Bifurcations in Optically Excited Nematic Liquid Crystals,” Phys. Rev. Lett., **83** 4744 - 4747 (1999).
- ⁵³J. Abshagen, G. Pfister, and T. Müllin, “Gluing Bifurcations in a Dynamically Complicated Extended Flow,” Phys. Rev. Lett, **87**, 224501 (2001).
- ⁵⁴T. Peacock and T. Mullin, “Homoclinic bifurcations in a liquid crystal flow,” J. Fluid. Mech. **432**, 369-386 (2001).
- ⁵⁵J. H. P. Dawes “Pattern selection in oscillatory rotating convection,” Physica D **147**, 336-351 (2000).